Chapter 6

Selection of Photonic Events with Missing Energy

In this chapter I present the methods that I have used to select and reconstruct photonic events with missing energy. I also describe how I suppressed background contributions and took into account various detector effects.

In the Standard Model of the electroweak interactions, single- or multi-photon events with missing energy could only be produced via the reaction $e^+e^- \rightarrow \nu\bar{\nu}\gamma(\gamma)$, as described in Chapter 2, Section 2.2. Such events were reconstructed using the precisely calibrated BGO electromagnetic calorimeter (see the previous chapter). However, in order to maximize the selection efficiency and minimize systematic errors, I used all other main subdetectors of L3 to perform studies of several detector effects and physics processes. I describe this work in more detail in the following sections. This work included studies of the forward calorimeters, BGO trigger efficiency and hermeticity, photon conversion, and detector noise. Also addressed are the problems of background suppression and cosmic contamination.

At the end of this chapter and in Appendix D, I describe the selected event samples and the corresponding selection efficiencies. In the next chapter I will use these data to measure the neutrino production at LEP and to search for manifestations of physics beyond the Standard Model.

6.1 Data and Monte Carlo Samples

Data collected by the L3 detector at LEP in the years from 1998 through 2000 were considered. They corresponded to the highest energy and luminosity LEP runs taken

Year	$\sqrt{s}$ (GeV)	Named as	$\mathcal{L}$ (pb^{-1})
1998	188.6	189	176.0
1999	191.6	192	29.5
	195.5	196	83.9
	199.5	200	81.3
	201.7	202	34.8
2000	202.5−205.5	205	74.8
	205.5−207.2	207	130.2
	207.2−209.2	208	8.6

Table 6.1: Center-of-mass energies, naming conventions, and corresponding integrated luminosities for the L3 data used in my analysis.

at center-of-mass energies $\sqrt{s} = 188.6 - 209.2$ GeV. Each year an integrated luminosity of approximately 200 pb^{-1} was collected, giving a total of 627 pb^{-1}. A detailed description of LEP performance was given in Chapter 4, Section 4.1.2.

Severe malfunctioning of the detector components crucial for my analysis could have a very large effect on the characteristics and rate of accepted events. Moreover, such time-dependent hardware problems were difficult to incorporate in the detector simulation. Therefore, to reduce systematic uncertainties related to the performance of the detector, I rejected both data and Monte Carlo events in the runs during which any of the main L3 subdetectors,[1] the energy trigger, and the global data acquisition system were not operating normally. As a result, the integrated luminosity I used in my analysis was reduced by about 1.3%, giving a total of about 619 pb^{-1}. The LEP data were divided into eight subsets according to the center-of-mass energy. The corresponding integrated luminosities and the naming conventions are listed in Table 6.1.

I rely on Monte Carlo simulations to optimize my selection cuts and to estimate the effects of my event reconstruction and the purity and efficiency of my selection. While modern Monte Carlo programs are extremely detailed and accurate, they are

---

[1] The main subdetectors of L3 did not include the muon filter and the VSAT.

not perfect. Therefore, any opportunity to double check a measurement or correction depending on the Monte Carlo simulations was exploited. The Monte Carlo generators that I used to simulate the relevant Standard Model processes are listed below.

The production of the photonic events with missing energy via initial-state radiation in the neutrino pair-production process, $\mathrm{e^+e^-} \rightarrow \nu\bar{\nu}\gamma(\gamma)$, was simulated using the `KKMC` [17] and `NUNUGPV` [27] MC generators. They were studied in Chapter 2 Section 2.2.3 and described in detail in Appendix A.

The large-angle (back-to-back) Bhabha scattering process and the di-photon production process, $\mathrm{e^+e^-} \rightarrow \gamma\gamma(\gamma)$, were simulated using the `BHWIDE` [156] and `GGG` [157] programs, respectively. I have already used these two generators in my studies of the BGO performance (see Section 5.6.2 of Chapter 5). In this chapter, I use events from these processes to study the efficiency of my event selection. In addition, the di-photon production process constituted the dominant source of background for the multi-photon channel.

The small-angle Bhabha scattering process, $\mathrm{e^+e^-} \rightarrow \mathrm{e^+e^-}\gamma(\gamma)$, was simulated using the `TEEGG` MC generator [168]. In this process, one or more particles were scattered at very low polar angles and typically escaped undetected along the beam pipe. This reaction could result in three event topologies according to the type of particles scattered at large polar angles: single-photon, single-electron, and electron-photon.[2] The single-photon Bhabha events constituted the main source of background for the single-photon channel. The single-electron events, where only one electron[3] was seen in the BGO, allowed me to study the trigger and scintillator efficiency as well as the performance of the forward calorimeters. It should be noted that the cross section of the single-electron process was more than ten times higher than the cross section of the single-photon and electron-photon radiative Bhabha scattering processes combined (see Table 6.2).

The four-fermion production processes $\mathrm{e^+e^-} \rightarrow \mathrm{e^+e^-}\nu\bar{\nu}(\gamma)$ and $\mathrm{e^+e^-} \rightarrow \mathrm{e^\pm}\ell^\mp\nu_\mathrm{e}\nu_\ell(\gamma)$

---

[2] The small-angle Bhabha scattering process, where the electron or positron is not detected, is also known as Compton scattering. It has recently been measured by L3 [171].

[3] Unless otherwise stated, in this chapter the word "electron" is used for both electrons and positrons.

$e^+e^- \rightarrow$	MC Generator	σ(pb)	Events	Phase-Space Cuts
$\nu\bar{\nu}(\gamma)$	`KKMC` [17]	57.52	540K	—
$\nu\bar{\nu}\gamma(\gamma)$	`NUNUGPV` [27]	13.09	200K	$E_{\gamma_1} > 0.8$ GeV $\theta_{\gamma_1} > 1.35^\circ$
$e^+e^-(\gamma)$	`BHWIDE` [156]	1,286	599K	$\theta_{e_{1,2}} > 8^\circ$
$e^+e^-\gamma(\gamma)$	`TEEGG` [168]	174.3	120K	$E_\gamma > 0.9$ GeV $\theta_\gamma > 13.5^\circ$ $\theta_{e_{1,2}} < 11^\circ$
		3,027	425K	$E_{e_2} > 0.9$ GeV $\theta_{e_2} > 13.5^\circ$ $\theta_{\gamma,e_1} < 11^\circ$
		95.9	70K	$E_{\gamma,e_2} > 0.1$ GeV $\theta_{\gamma,e_2} > 10^\circ$ $\theta_{e_1} < 5^\circ$
$\gamma\gamma(\gamma)$	`GGG` [157]	18.3	75K	$\theta_{\gamma_{1,2}} > 5^\circ$
$e^+e^-\nu\bar{\nu}$	`EXCALIBUR` [169]	0.50	20K	$\theta_{e_1} > 5.1^\circ$
$e^\pm\ell^\mp\nu_e\nu_\ell$		1.09	40K	$\ell = \mu, \tau$
$e^+e^-e^+e^-$	`DIAG36` [170]	705	600K	$m_{e_3e_4} > 3.1$ GeV $\theta_{e_{3,4}} > 10^\circ$
$\tau^+\tau^-(\gamma)$	`KORALZ` [22]	6.8	15K	—

Table 6.2: Standard Model processes, Monte Carlo programs, cross sections within the indicated kinematic regions and the size of the corresponding event samples. All events were generated at $\sqrt{s} = 207$ GeV. The three lines for the radiative Bhabha process correspond to the single-photon, single-electron, and electron-photon event topologies, respectively.

were simulated using the `EXCALIBUR` MC generator [169]. These processes also provided an important source of background for my selection. Finally, the reactions $e^+e^- \rightarrow e^+e^-e^+e^-(\gamma)$ and $e^+e^- \rightarrow \tau^+\tau^-(\gamma)$ were simulated using the `DIAG36` [170] and `KORALZ` [22] programs, respectively.

The Monte Carlo programs that I used are summarized in Table 6.2, which lists the production cross sections, the size of the corresponding event samples, and the phase-space cuts used during the event generation.

The L3 detector response was simulated using the `GEANT` program [127], which described effects of energy loss, multiple scattering, and showering in the detector. Time-dependent detector inefficiencies,[4] as monitored during the data taking period, were included in the simulation. It should be noted that during the last three years of the LEP program (1998-2000), the configuration and performance of the L3 detector were very stable. In particular, the number and the location of the dead channels, the

---

[4] Such detector inefficiencies included the position of the dead or noisy channels in the calorimeters and the location of the disconnected sectors in the TEC and muon chambers.

accuracy of the subdetector calibrations, and the trigger thresholds remained essentially unchanged. Therefore, in most of my detector studies, I regarded these three years as a single data-taking period.[5] Additional cross checks showed no significant year-to-year variation in the selection efficiency related to the detector effects.

6.2 Event Topologies

Electrons and photons were reconstructed using the BGO electromagnetic calorimeter,[6] whose barrel and endcaps subtended the polar angle ranges $43^\circ < \theta < 137^\circ$ and $10^\circ < \theta(180^\circ - \theta) < 37^\circ$, respectively. In order to discriminate between photons and electrons, I used information from the tracking chamber (TEC) whose efficiency decreased rapidly at low polar angles. Therefore, I applied an additional cut on the photon polar angle, $14^\circ < \theta < 166^\circ$.

The main background came from radiative Bhabha scattering, $\mathrm{e}^+\mathrm{e}^-\rightarrow\mathrm{e}^+\mathrm{e}^-\gamma$, where both electrons were lost in the beam pipe, and only a photon was scattered at a large polar angle. Such events could be rejected by requiring the transverse momentum of the photon to be above $0.02\sqrt{s}$, as shown in Figure 6.1. This cut ensured that at least one of the scattered electrons could be detected by the forward calorimeters.

The single- and multi-photon events were triggered by the BGO energy triggers, as described in Section 4.2.9. In the barrel and endcap regions, the thresholds of these triggers were set at about 1.5 GeV and 7 GeV, respectively.

The above conditions determined the three event topologies that I considered in my analysis:

- **Single-photon events:** a photon with $14^\circ < \theta_\gamma < 166^\circ$ and $P_t^\gamma > 0.02\sqrt{s}$. There should be no other photon with $E_\gamma > 1$ GeV.

- **Multi-photon events:** at least two photons with $E_\gamma > 1$ GeV, with the most energetic in the region $14^\circ < \theta_\gamma < 166^\circ$ and the other in the region

---

[5] This approach was used in the majority of the L3 analyses at LEP2.

[6] The performance and the calibration of the BGO calorimeter were described in detail in Chapter 4, Section 4.2.3 and in Chapter 5.

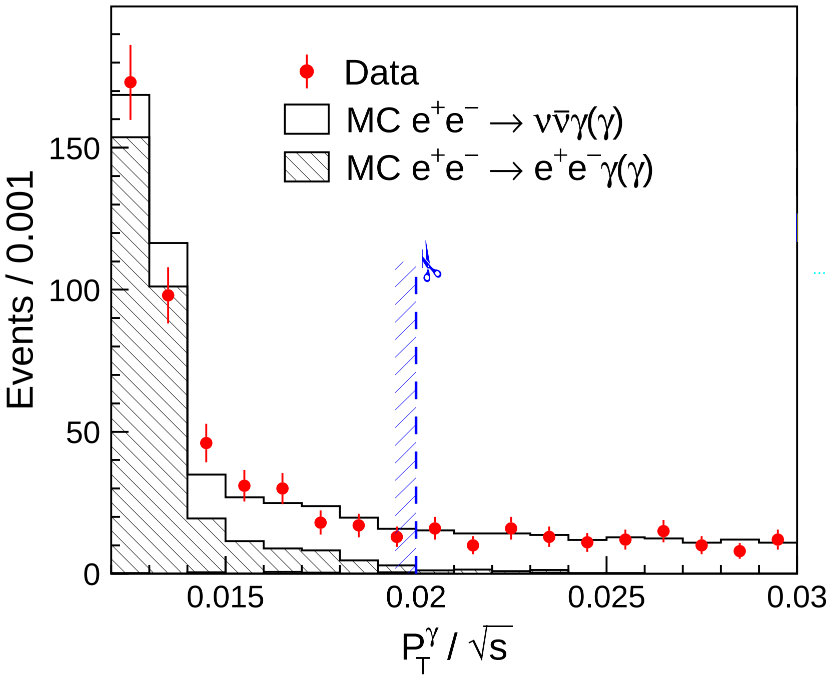

Figure 6.1: Transverse momentum distribution for the single-photon events after all other selection cuts have been applied. The dashed line indicates the position of the cut $P_t^\gamma > 0.02\sqrt{s}$. Only the region of interest is shown.

$12° < \theta_\gamma < 168°$. The transverse momentum of the multi-photon system should satisfy $P_t^{\gamma\gamma} > 0.02\sqrt{s}$.

- **Soft-photon events:** a photon in the barrel region ($43° < \theta_\gamma < 137°$) with $0.008\sqrt{s} < P_t^\gamma < 0.02\sqrt{s}$. There should be no other photon with $E_\gamma > 1$ GeV.

The selected sample of the single- and multi-photon events was dominated by events from the process $\mathrm{e^+e^-} \to \nu\bar{\nu}\gamma(\gamma)$. Thus, it could be used to study the cross section of this process and to measure the number of light neutrino species. In the next chapter I will also use this event sample to search for manifestations of Physics beyond the Standard Model, such as extra dimensions, Supersymmetry, and anomalous boson couplings.

In the region of the soft-photon event topology, most of the selected events were expected to be due to the small-angle Bhabha scattering process, $\mathrm{e^+e^-} \to \mathrm{e^+e^-}\gamma(\gamma)$. The inclusion of the soft-photon sample significantly increased the sensitivity of my searches for extra dimensions and pair-produced gravitinos.

For a large fraction of the single- and multi-photon events, emission of the ISR photons reduced the effective center-of-mass energy of the e^+e^- pair to the Z resonance, as described in Section 2.2.2. This phenomenon is called the *radiative return to the Z*. Thus, the distribution of the recoil mass to the photon system (M_{rec}) was expected to peak around the Z mass. Since this effect did not depend on the value of $\sqrt{s}$, instead of using the photon energy variable I usually used the photon recoil mass, defined as

$$M_{\mathrm{rec}} = \sqrt{\left(\sqrt{s} - E_\gamma\right)^2 - |\vec{p}_\gamma|^2}\,, \tag{6.1}$$

where $E_\gamma = \sum_i E_{\gamma_i}$ and $\vec{p}_\gamma = \sum_i \vec{p}_{\gamma_i}$ are the total energy and momentum of the photons. For the single-photon topology, Equation 6.1 becomes $M_{\mathrm{rec}} = \sqrt{s - 2\sqrt{s}E_\gamma}$.

6.3 Single-Photon Selection

The selection of the $e^+e^- \to \nu\bar{\nu}\gamma(\gamma)$ candidates aimed at identifying events with 1) one neutral electromagnetic energy deposit in the BGO calorimeter and 2) no other activity in the detector apart from what was consistent with noise. Below I describe the basic cuts of the single-photon selection and give a brief outline of the following sections in which these cuts and their performance will be discussed in more detail.

Photon candidates were required to have an energy greater than 1 GeV, and the shape of their energy deposition had to be consistent with an electromagnetic shower. This was ensured by a dedicated shower-shape analysis which is described in the next section. As defined in the previous section, the single-photon events were required to contain only one photon candidate with $14^\circ < \theta_\gamma < 166^\circ$ and $P_t^\gamma > 0.02\sqrt{s}$.

The single-photon events were triggered by the BGO trigger system, whose efficiency as a function of the shower energy is studied in Section 6.3.2.

The visible energy not assigned to the identified photon had to be less than 10 GeV, and the energy measured in the EGAP and HCAL calorimeters had to be less than 7 GeV each. There must be at most one ECAL cluster (bump) with an energy above 50 MeV not identified as a photon. Each BGO endcap had a hole at $\phi \simeq 270°$ and $\theta(180° - \theta) \simeq 16°$, which was required for the passage of the RFQ beam pipe (see Section 4.2.3). In order to eliminate the related background from mismeasured di-photon events, I rejected single-photon events with a photon in the region opposite to an RFQ hole.

To suppress background from the radiative Bhabha scattering process, events with a transverse momentum less than 15 GeV were rejected if an energy cluster was observed in the forward calorimeters with an acoplanarity[7] with the photon candidate less than 30°. Furthermore, if a photon was detected with an acoplanarity less than 15° with a hadron calorimeter cluster, the energy of that cluster had to be less than 3 GeV. The efficiency of these cuts is discussed in Section 6.3.3.

Electron candidates were removed by requiring that no charged track reconstructed in the central tracking system (TEC) matched the ECAL cluster. The probability of photon conversion in the beam pipe and in the silicon microvertex detector was about 5% in the barrel region and increased rapidly at low polar angles, reaching about 20% at $\theta \simeq 20°$. This effect is studied in Section 6.3.4.

The cosmic ray background was rejected using a set of dedicated anti-cosmic cuts, as described in Section 6.3.5. Finally, the problems of the BGO shower leakage and of the detector noise are studied in Sections 6.3.6 and 6.3.7, respectively. The selection results are presented in Section 6.3.8 and in Appendix D.

A typical single-photon event recorded by the L3 detector is shown in Figure 6.2. The recoil mass of this photon was measured to be consistent with the Z mass, $M_{\mathrm{rec}} = 92.6$ GeV. The cluster in the HCAL behind the BGO bump indicates a minor leakage of the electromagnetic shower into the hadron calorimeter. This figure also shows two additional low-energy deposits, in the opposite endcap of the HCAL and in the EGAP calorimeter. These two clusters were most probably faked by the detector noise.

---

[7] Acoplanarity is defined as the complement of the angle between the projections in the plane perpendicular to the beam axis.

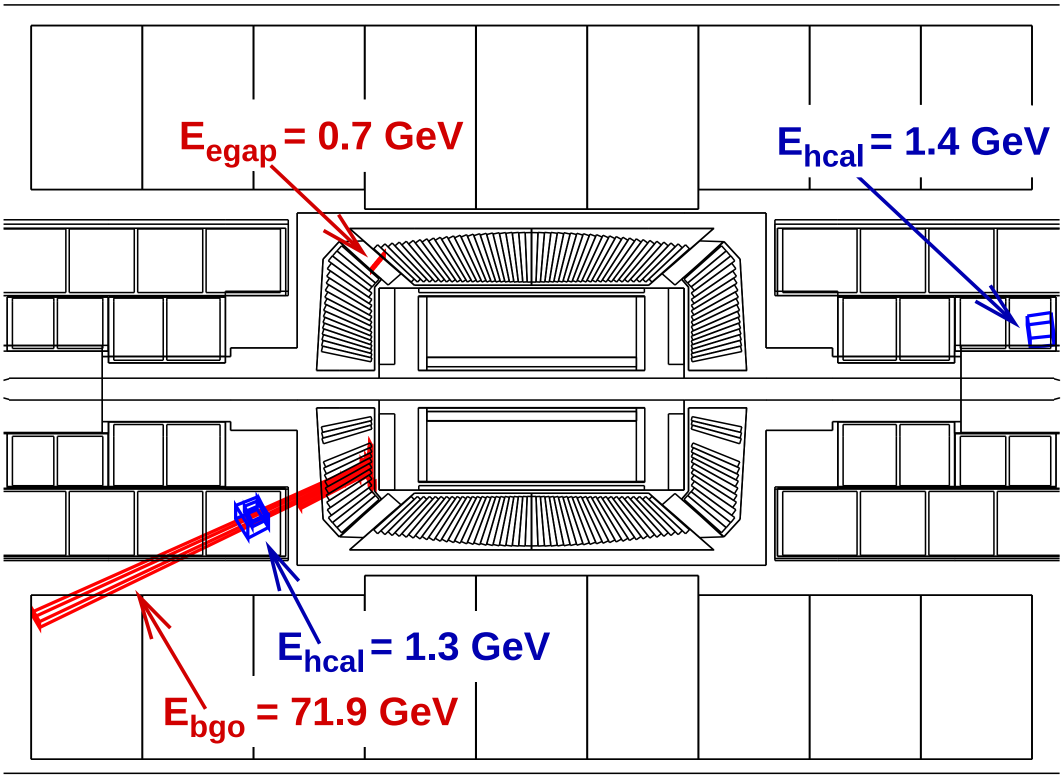

Figure 6.2: A typical single-photon event recorded by the L3 detector and displayed in the $y - z$ plane. This event was recorded in 1998 data at $\sqrt{s} =$ 189 GeV.

6.3.1 Shower-Shape Analysis

In order to ensure that the BGO shower of the photon candidate was consistent with an electromagnetic shower, I applied a set of cuts based on the measured shower profile. These *shower-shape* cuts not only ensured that the accepted photon showers were well measured in the BGO but also suppressed a large fraction of background due to cosmic rays and mismeasured events from other Standard Model processes.

The pattern of individual crystal energies in a BGO bump provides a transverse sampling of the shower that developed when a particle passed through the electromagnetic calorimeter (see Section 5.1). In the case of electrons and photons, the resulting shower had a transverse profile that did not depend strongly on the particle energy in the range $E \simeq 1 - 100$ GeV [172]. This transverse profile was characterized by two quantities, S_9^c/S_{25}^c and shower roundness, which are defined below. The longitudinal profile of the shower could be characterized by the ratio of energy deposited in the hadron calorimeter behind the BGO bump and the bump energy as measured by the BGO, $E_{\mathrm{HCAL}}/E_{\mathrm{BGO}}$.

In addition, about 20% of the selected showers were either near the calorimeter edges or had a dead channel in their 3×3 matrices (see Section 5.3.2). The resulting mismeasurement of the lateral shower profile was taken into account by relaxing the values of the cuts on shower roundness and S_9^c/S_{25}^c variable.

The S_9^c/S_{25}^c variable was defined as the ratio of the corrected sums of energies deposited in the 3×3 and 5×5 matrices centered on the bump crystal, where the individual S_9^c and S_{25}^c variables were defined by Equation 5.2 in Section 5.1. The electromagnetic BGO showers were almost fully contained in the 3×3 crystal matrix, and, in the case of electrons and photons, this ratio was expected to be close to one. Thus, I required that S_9^c/S_{25}^c should be greater than 0.94. It should be noted that this or similar cut values were widely used in L3 to reject showers originating from hadrons and cosmic rays. For showers with dead or missing crystals, this cut was relaxed to $S_9^c/S_{25}^c > 0.92$.

Photon candidates with significant leakage into the hadron calorimeter were rejected by requiring $E_{\mathrm{HCAL}}/E_{\mathrm{BGO}} < 0.2$, where E_{BGO} was the bump energy as measured by the BGO and E_{HCAL} was defined as a sum of energies of the HCAL clusters in a 10° cone around the photon direction. The longitudinal shower leakage also affected the BGO energy resolution. This problem is addressed in Section 6.3.6.

To further suppress events from cosmic rays, I used another quantity called shower roundness. It is defined as the ratio of the smallest and largest eigenvalues of the following tensor:

$$F^{\mu\nu} = \sum_i E_i x_i^\mu x_i^\nu \,, \tag{6.2}$$

where E_i is energy of the ith crystal, x_i^μ and x_i^ν are given in the local Cartesian coordinate system with the center of bump crystal at the origin, and the summation is performed over all crystals in the BGO bump [173]. The shower roundness can be interpreted as the ratio of the minor and major axes of an ellipse describing the transverse profile of the shower. For electrons and photons produced at the interaction point of L3, the transverse shower profiles were expected to have a circular shape, i.e., their shower roundness was expected to be close to one. On the contrary, BGO showers in cosmic ray events usually had small values of roundness since such showers corresponded to photons radiated by cosmic muons, and most of the cosmic muons traversed the BGO calorimeter at a significant angle with respect to the crystal axis. Thus, I required that the measured shower roundness should be greater than 0.4. For showers with dead or missing crystals, the value of this cut was relaxed to 0.2.

The efficiency of the shower-shape selection was measured using large samples of di-photon, back-to-back Bhabha, and single-electron Bhabha events which were selected in the 1998-2000 data. The agreement between data and Monte Carlo simulations was checked using the large samples of MC events from the corresponding Standard Model processes. These three Standard Model processes were chosen because they provided very distinct and clean signatures so that little or no contamination was expected from hadronic events or cosmic rays.

The di-photon and back-to-back Bhabha events were selected using the same selection criteria[8] as the ones described in Section 5.6.2, where I discussed the absolute calibration of the BGO calorimeter using Bhabha events. The di-photon subsample was further selected by requiring no significant activity in the TEC. In the high-energy LEP runs at $\sqrt{s} = 189 - 208$ GeV, I selected samples of about 3,400 and 130,000 di-photon and back-to-back Bhabha events, respectively. In addition, I selected about 30,000 Bhabha events in the calibration data at the Z peak, $\sqrt{s} = 91.3$ GeV. Figure 6.3 shows the distributions of the shower-shape variables for the Bhabha events selected in the Z-peak data. While the distributions of the S_9^c/S_{25}^c and roundness variables demonstrated a good agreement between data and Monte Carlo, the $E_{\mathrm{HCAL}}/E_{\mathrm{BGO}}$ distributions indicated that the detector simulation underestimated the longitudinal shower leakage.

---

[8] Except that I did not apply any cuts on the shower shape. In addition, I only used showers with a polar angle $\theta_{shower} > 14°$, i.e., in the fiducial angular region of my photonic selections.

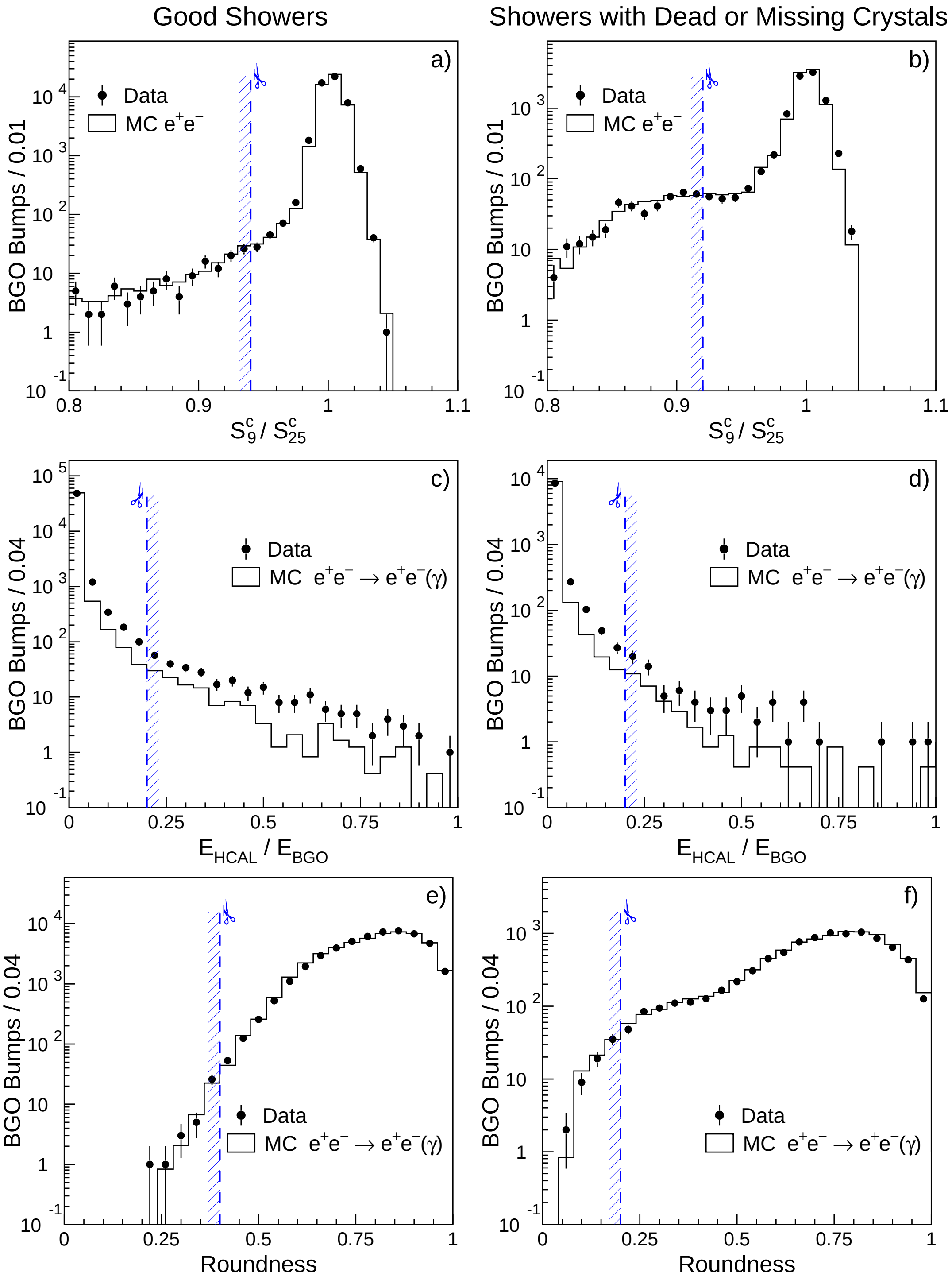

Figure 6.3: Distributions of a,b) S_9^c/S_{25}^c, c,d) $E_{\mathrm{HCAL}}/E_{\mathrm{BGO}}$, and e,f) shower roundness for Bhabha events from the 1998-2000 Z-peak calibration data, after all other shower-shape cuts have been applied (barrel and endcaps combined). The dashed lines indicate the values of the cuts. The distributions for the good bumps and for the bumps with a dead crystal or near the detector edges are shown on the left and right side, respectively.

As I defined in the previous section, the single-electron events were radiative Bhabha scattering events where one electron and a photon had a very low polar angle and only a low energy electron was scattered at a large polar angle. Such events were selected by requiring a single shower in the BGO with a matching track in the TEC and a matching cluster in the forward calorimeters. The polar angle of the single-electron candidate was required to be above 14°, which corresponded to the fiducial region of my photonic selections. The energy of the matching cluster had to be greater than 50 GeV and its acoplanarity with the single-electron candidate less than 10°. There should have been no other activity in the detector apart from what was consistent with noise. The selected events must also satisfy the anti-cosmic cuts defined in Section 6.3.5. To study the efficiency of the shower-shape selection, only showers with an energy $E_{\mathrm{BGO}} = 7.5 - 12.5$ GeV were chosen. In total, I selected about 85,000 such single-electron events.

The large statistics back-to-back and single-electron Bhabha samples allowed a precise measurement of the shower-shape selection efficiency for electrons with energies $E_{\mathrm{BGO}} \simeq 10, 45$, and 100 GeV. This was important because the energy of the single-photon showers varied between about 5 and 90 GeV, with an average value of $< E_\gamma >= 54$ GeV. In addition, the di-photon sample provided a direct comparison between the showers originating from electrons and photons.

The obtained values of the shower-shape selection efficiency are quoted in Table 6.3. It shows that for all shower energies and types, the efficiency was slightly higher for the MC simulation. This effect was explained by the inaccurate simulation of the longitudinal shower leakage (see Figures 6.3c,d) and was corrected by scaling down the numbers of expected events by a common factor of approximately -0.3%. After this correction, a good agreement between the data and the Monte Carlo simulations was observed. It should be noted that the selection performance was almost the same for the showers in the barrel and in the endcaps. In addition, the selection efficiency for the photon showers was found to be only about 0.2% smaller than that for the electron showers (at 100 GeV). This result was also in good agreement with the predictions of the Monte Carlo simulation. In the case of 45 GeV electrons, the

Production Process and Average Particle Energy		Efficiency of the Shower-Shape Selection [%]		
		Good Bumps		Bumps with Dead or Missing Crystals
		Barrel	Endcaps	
Bhabha Scattering $E_{\mathrm{e}} = 100$ GeV	Data	99.36 ± 0.05	99.13 ± 0.02	94.8 ± 0.1
	MC	99.54 ± 0.03	99.47 ± 0.01	95.3 ± 0.1
Di-Photon $E_{\gamma} = 100$ GeV	Data	98.92 ± 0.20	99.17 ± 0.16	95.2 ± 0.6
	MC	99.38 ± 0.05	99.32 ± 0.05	95.9 ± 0.2
Bhabha Scattering $E_{\mathrm{e}} = 45$ GeV	Data	99.16 ± 0.07	99.01 ± 0.06	94.3 ± 0.2
	MC	99.45 ± 0.03	99.36 ± 0.03	94.7 ± 0.1
Single Electron $E_{\mathrm{e}} = 10$ GeV	Data	97.94 ± 0.11	98.11 ± 0.06	93.4 ± 0.2
	MC	98.40 ± 0.07	98.23 ± 0.04	93.5 ± 0.1

Table 6.3: Efficiency of the shower-shape selection as measured for different shower energies and types.

efficiency of the shower-shape selection was measured to be about 99.1% for the good showers and 94.3% for the showers with a dead crystal or near the detector edges.

6.3.2 Trigger Efficiency

A good understanding of the trigger performance was required for a precise measurement of the single- and multi-photon production. In this section I describe a study of the trigger efficiency that I performed using Bhabha scattering events.

Events with only photons in the final state could be triggered only by the BGO energy triggers which were described in detail in Section 4.2.9. These triggers included the single-photon (barrel only), the BGO cluster, and the total energy triggers with thresholds at about 1.5, 7, and 30 GeV, respectively.

Near the threshold, the performance of the BGO triggers could be monitored using a dedicated, independent trigger called single-electron trigger [173]. This trigger required a coincidence between a cluster in one of the luminosity monitors and a track in the TEC. Thus, it could be used to select an independent sample of single-electron Bhabha events (as follows from its name). The efficiency of the single-electron trigger had been measured to be 98.5% [173].

The basic selection of single-electron Bhabha events was described in the previous section. In addition, such events were required to be triggered by the single-electron trigger. The energy of the single-electron showers was required to be above 1 GeV in the BGO barrel and 5 GeV in the endcaps. Furthermore, there had to be no other bump in the BGO with an energy above 0.5 GeV. In 1998-2000 data, I selected a total of about 76,000 and 27,000 single-electron events in the BGO barrel and endcaps, respectively. The corresponding energy spectra are shown in Figures 6.4a,c.

These independently triggered single-electron events could then be used to measure the efficiency of the BGO triggers by checking whether or not these triggers were also activated. Figures 6.4b,d show the obtained BGO trigger efficiency as a function of the shower energy together with the corresponding Monte Carlo prediction. In the barrel it rises sharply at the energy threshold of the single-photon trigger and reaches a plateau mainly determined by the efficiency of the corresponding trigger algorithm. With increasing energy additional triggers became active, resulting in a second threshold rise and a final plateau at about 8 GeV in the barrel and 10 GeV in the endcaps.

The trigger efficiencies in the plateau regions were determined by fitting the obtained efficiency curves to a straight line. In the case of the barrel, a fit in the plateau region $E_{\mathrm{BGO}} = 8 - 16$ GeV gave a value of $93.1 \pm 0.6\%$ for the data and $94.5 \pm 0.2\%$ for the Monte Carlo prediction. In the case of the endcaps, I fitted the plateau region $E_{\mathrm{BGO}} = 10 - 25$ GeV, and the corresponding efficiencies were determined to be $95.7 \pm 0.4\%$ and $97.5 \pm 0.1\%$ for the data and Monte Carlo, respectively. These measurements were in good agreement with the results of an earlier study performed using 1998-1999 data [120].

The main contribution to the trigger inefficiency was due to the presence of inactive trigger channels. About 4.7% of the trigger channels in the barrel and 2% of the channels in the endcaps were flagged as inactive, both during the data taking and during the detector simulations. The location of the inactive channels was well known and stable during the considered period of 1998-2000. No significant time-dependent

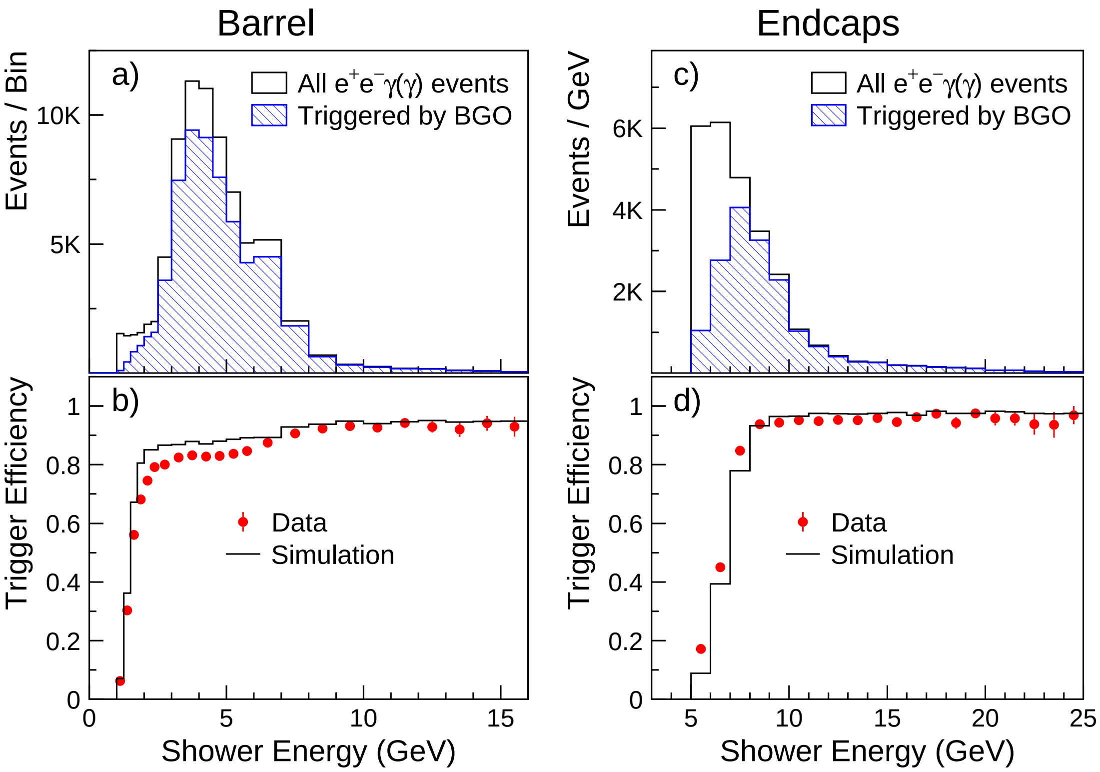

Figure 6.4: Energy spectra of the single-electron events a) in the barrel and c) in the endcaps. Trigger efficiency curves as a function of the shower energy b) for the BGO barrel and d) for the BGO endcaps.

variations in the measured trigger efficiency were found.

Additional factors causing trigger inefficiency included detector noise and finite ADC resolution. These effects were not taken into account during the simulation of the detector response [173]. As demonstrated above, the Monte Carlo simulation overestimated the trigger efficiency in the plateau regions by about 1.5%, both for the barrel and the endcaps. Moreover, for showers with energies near the trigger thresholds, the relative difference between data and Monte Carlo was energy-dependent and could be as high as 20%, as shown in Figures 6.4b,d. As a result, the trigger efficiency in the simulation had to be adjusted to eliminate this discrepancy between data and Monte Carlo.

The measured efficiency curves could not be directly applied to the Monte Carlo simulation of the $e^+e^- \rightarrow \nu\bar{\nu}\gamma$ process since its differential cross section differed from that of the single-electron Bhabha scattering. Therefore, I computed the efficiency curves separately for each of the four $|\cos\theta|$ slices[9] in the barrel and in the endcaps so that the applied correction factors depended on both the shower energy and polar angle.

Figures 6.4a,c show that the cross section of single-electron production decreased rapidly with the single-electron energy. Therefore, I performed a complementary study of the trigger performance at high energies using back-to-back Bhabha events. Such Bhabha events could be independently triggered by the TEC trigger, whose efficiency was found to be about 97% [135]. To measure the efficiency of the BGO triggers, I selected a subsample of such events from the Bhabha sample obtained using the calibration data at the Z peak (see the previous section). With these events, the BGO trigger efficiency was measured to be $99.57 \pm 0.07\%$ in the barrel and $99.72 \pm 0.04\%$ in the endcaps. After applying the correction factors derived using the single-electron events, the corresponding trigger efficiencies for the MC simulation were found to be $99.63 \pm 0.04\%$ and $99.74 \pm 0.03\%$. Good agreement between data and Monte Carlo was observed. In addition, these measurements are consistent with the results of a similar study described in Reference [135].

6.3.3 Background Rejection

The single-photon topology of the radiative Bhabha scattering process, $e^+e^- \rightarrow e^+e^-\gamma$, was by far the most copious source of background in my selection of single-photon events. In this process, the incoming electrons were scattered at low polar angle (typically with energies close to the beam energy) and only the radiated photon was detected in the BGO. Such events are referred to as single-photon Bhabha events.

The lower cut on the photon transverse momentum, $P_t^\gamma > 0.02\sqrt{s}$, ensured that at least one of the two electrons was scattered at a significant angle with respect to the beam axis so that it could be detected in the forward calorimeters. As a result, this source of background could be almost completely suppressed by the veto cuts that I

---

[9] The granularity of the BGO trigger system was described in Section 4.2.9.

describe below. Since the differential cross section of the radiative Bhabha scattering peaked at low values of P_t^γ [168], I applied tighter cuts in the region of low transverse momentum.

For single-photon candidates with a transverse momentum less than 15 GeV, I required that no energy cluster be observed in the forward calorimeters with an acoplanarity with the photon candidate less than 30° (the definition of the acoplanarity was given in footnote 7 on p. 138). As described in Sections 4.2.7 and 4.2.8, the forward calorimeters of L3 covered the polar angle range of $1.4^\circ < \theta(180^\circ - \theta) < 8.7^\circ$ and consisted of the active lead rings (ALR) and the luminosity monitors (LUMI). The upper cuts on the energy of such clusters were set at $E_{\mathrm{ALR}} < 0.1$ GeV and $E_{\mathrm{LUMI}} < 1$ GeV.

To minimize the inefficiencies caused by the detector noise, this cut was relaxed to $E_{\mathrm{ALR,LUMI}} < 60$ GeV for single-photon candidates with $P_t^\gamma > 15$ GeV. This did not increase the background contamination since in radiative Bhabha events with such high values of P_t^γ at least one of the electrons was expected to be scattered into a region covered by the BGO or HCAL endcaps. Such events were rejected by the veto cuts on energy depositions in the HCAL and the BGO.

Figures 6.5a,b show the distributions of energies deposited in the LUMI and ALR calorimeters for single-photon candidates with $P_t^\gamma < 15$ GeV before the corresponding cuts were applied. In total, I selected 9,506 such events in data with about 9,362.3 expected from Monte Carlo. Only about 5% of the MC expectation was due to the genuine single-photon production process, $\mathrm{e}^+\mathrm{e}^- \rightarrow \nu\bar{\nu}\gamma$.

Figures 6.5c demonstrates that radiative Bhabha events with a cluster in the LUMI calorimeter could be almost completely suppressed by applying a veto cut $E_{\mathrm{LUMI}} < 1$ GeV. In the case of the ALR energy spectrum, a large fraction of events had $E_{\mathrm{ALR}} < 5$ GeV, as shown in Figure 6.5d. For such events I applied a tighter cut $E_{\mathrm{ALR}} < 0.1$ GeV.

The origin of this effect can be understood by reconstructing the polar angle of the electron scattered into the ALR (θ_{tag}). Because the second electron was almost always scattered parallel to the beam axis, the θ_{tag} angle could be estimated using only the energy and polar angle of the photon detected in the BGO. The exact formula

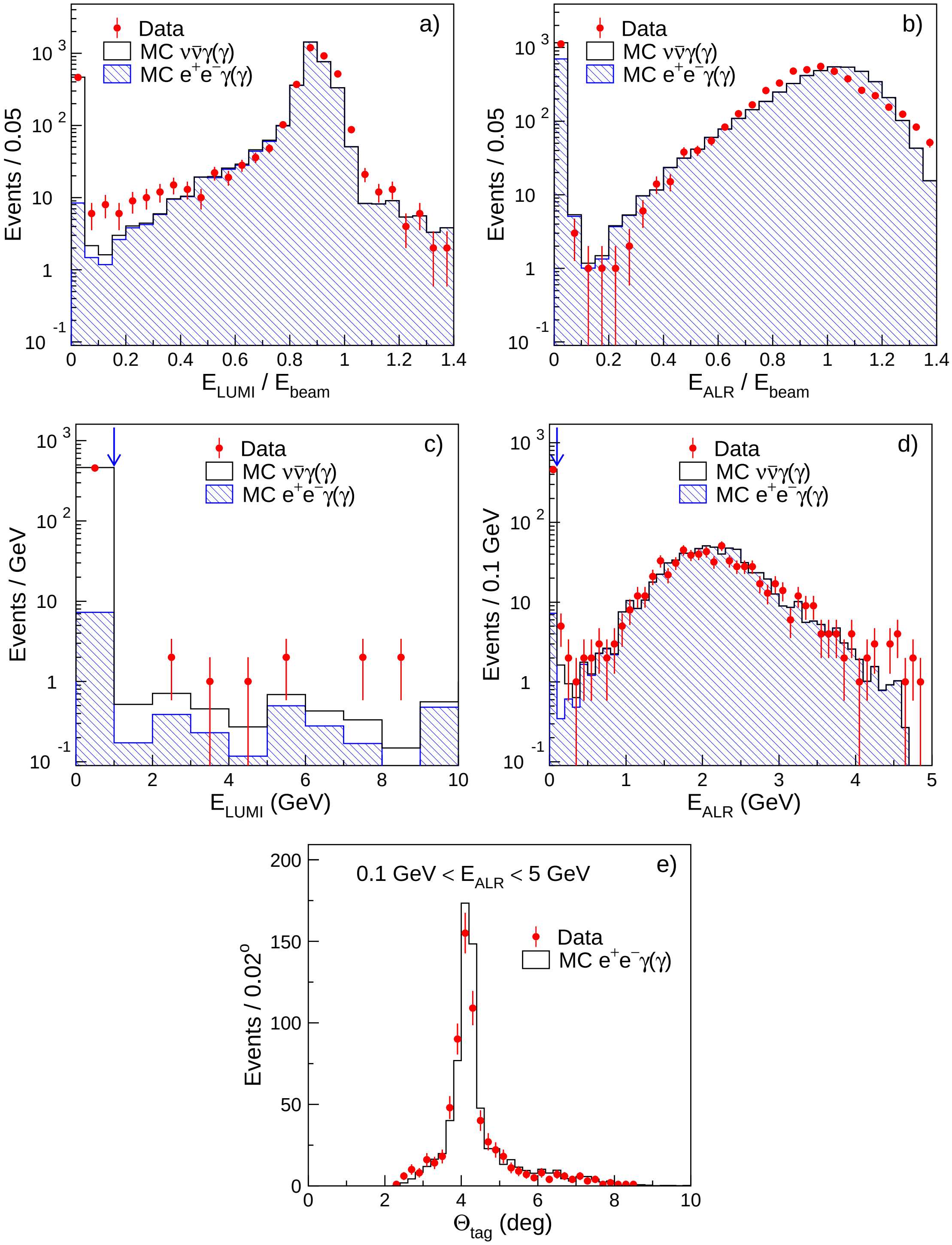

Figure 6.5: Distributions of the energies measured a) in the LUMI and b) in the ALR forward calorimeters scaled to the beam energy before the corresponding veto cuts are applied. Energy measured c) in the LUMI and d) in the ALR calorimeters for the regions of interest $E_{\rm LUMI} < 10$ GeV and $E_{\rm ALR} < 5$ GeV, respectively. The arrows indicate the values of the cuts. e) Distribution of the θ_{tag} angle for events with $0.1 < E_{\rm ALR} < 5$ GeV.

will be quoted in the following. Figure 6.5e shows the distribution of the θ_{tag} angle reconstructed for single-photon candidates with $0.1 < E_{\mathrm{ALR}} < 5$ GeV. A clear peak at $\theta_{tag} \simeq 4^\circ$ was observed which corresponded to the region of the lower edge of the ALR calorimeter. Figure 6.5e also shows that this effect was well reproduced in simulations of the detector response.

Tagging Efficiency of the Forward Calorimeters

In order to cross check the veto efficiency of the above cuts, I selected a sample of single-electron events. I applied the same cuts as for the selection of the single-electron sample used in the trigger studies (see the previous section). However, only events in the BGO barrel and triggered by the BGO triggers were accepted. In addition I did not require a matching cluster in the forward calorimeters. In order to suppress background from cosmic rays, the TEC track matched to the BGO shower had to pass certain quality criteria.[10]

The single-electron Bhabha events were previously defined as events in which only one electron was observed in the BGO, and the second electron and the radiated photon were scattered at low polar angles. In most of the such events, one of the two particles (electron or photon) was scattered at a very small polar angle and could be assumed to be parallel to the beam axis, as schematically shown in Figure 6.6.

Under this assumption, the polar angle of the particle scattered at a low, but non-negligible, polar angle can be calculated as

$$\cos\theta_{tag} = \frac{a^2 - 1}{a^2 + 1}, \text{ with } a = \frac{2\,E_{\mathrm{beam}}}{E_{bgo}\,\sin\theta_{bgo}} - \frac{1 + \cos\theta_{bgo}}{\sin\theta_{bgo}}, \tag{6.3}$$

where E_{bgo} and θ_{bgo} are the energy and polar angle of the electron observed in the BGO calorimeter. In the phase-space region of the single-photon topology, $\theta > 14^\circ$ and $P_t > 0.02\sqrt{s}$, the θ_{tag} angle is constrained to be above about 2.3°.

For my study of the tagging efficiency, I selected a subsample of about 80,000

---

[10] These quality criteria were: transverse momentum of the track greater than 100 MeV; its distance of closest approach to the interaction point (DCA) less than 10 mm; the number of used wire hits more than 14; the number of wires between the first and last hit at least 15.

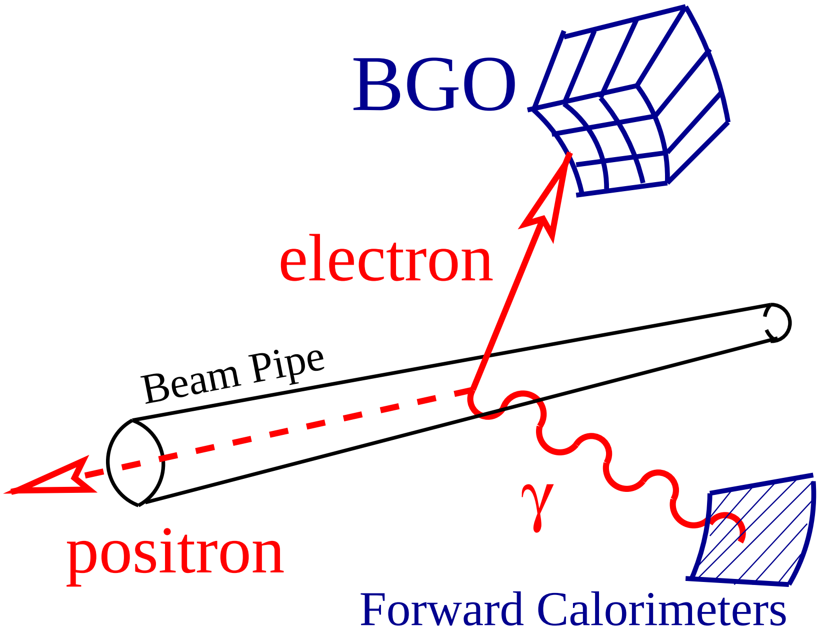

Figure 6.6: Schematic diagram of a single-electron event tagged by one the forward calorimeters.

single-electron events with $1.4^\circ < \theta_{tag}(180^\circ - \theta_{tag}) < 7.5^\circ$. The corresponding θ_{tag} distribution is shown in Figure 6.7a. The tagging efficiency of the forward calorimeters was then calculated as a ratio of the number of events not passing the veto cuts to the total number of single-electron events. The veto cuts on the energy in LUMI and ALR were the same as the ones used in the single-photon selection (see above).

Figure 6.7b compares the obtained veto efficiency as a function of the θ_{tag} angle with the Monte Carlo prediction. In the region of θ_{tag} values compatible with the single-photon event topology, $2.3^\circ < \theta_{tag}(180^\circ - \theta_{tag}) < 7.5^\circ$, the veto efficiency was measured to be $\varepsilon_{veto} = 99.74 \pm 0.03\%$ for the data and $\varepsilon_{veto} = 99.77 \pm 0.02\%$ for the simulation.

I also used the θ_{tag} variable to remove background due to inactive sectors in the HCAL endcaps, where particles escaped undetected. These sectors were located in the azimuthal angle intervals of 82° – 96° and 262° – 276°. In my event selection, the HCAL endcaps were used as veto detectors only in a small gap between the ALR and the BGO endcaps ($8.7^\circ < \theta < 10^\circ$). Therefore, both the single-photon and the

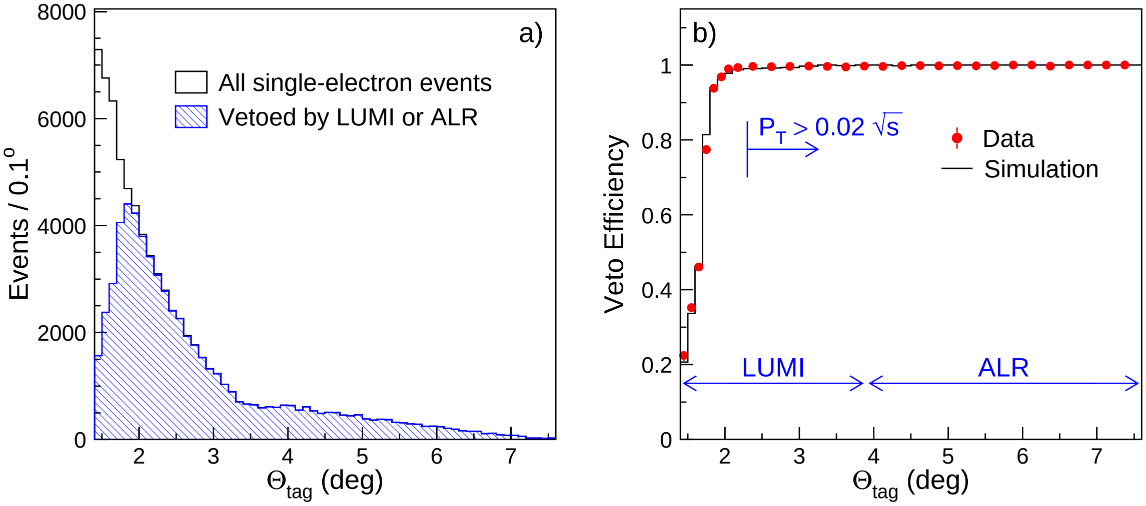

Figure 6.7: a) Distribution of the θ_{tag} angle for the selected single-electron events. b) Veto efficiency as a function of θ_{tag} obtained using this event sample. Events with $\theta_{tag} > 90°$ are included using $\theta_{tag} \rightarrow 180° - \theta_{tag}$.

single-electron candidates, detected in these ϕ-ranges, were discarded only if they had $7° < \theta_{tag}(180° - \theta_{tag}) < 12°$.

6.3.4 Photon Conversion

Electron candidates were removed by requiring that the number of hits in the TEC within an azimuthal angle of $\pm 8°$ around the path of the photon candidate must be less than the 40% of that expected for an electron, $N_{hits}/N_{exp} < 0.4$. The discrimination power of this cut on TEC occupancy was well tested by other physics analyses of L3. For example, it was used in the "official" L3 studies of the di-photon [158] and Bhabha [135] production processes.

This brings us to the problem of photon conversion. A significant fraction of photons converted into an e^+e^- pair before entering the L3 tracker. Figure 6.8 shows that such events would in general be rejected by the above cut on the TEC occupancy. In this section I describe my measurement of the photon conversion rates and my selection of the converted photons.

The probability for a photon to convert after traversing a length ℓ of material is

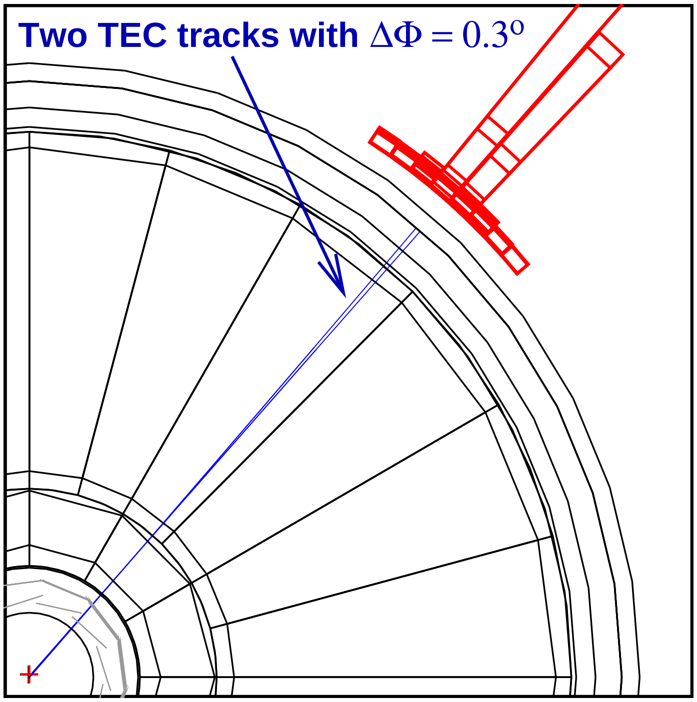

Figure 6.8: A photon conversion candidate. The two matching tracks are separated by about 0.3° in azimuth.

given by

$$P_{conv} = 1 - \exp(-\ell/[9/7X_0])\,, \tag{6.4}$$

where X_0 is the radiation length of this material. This equation is expected to be accurate to within a few percent down to photon energies as low as 1 GeV [6]. As a cross check, I studied the energy dependence of the conversion probability using the detector simulation program of L3. The $P_{conv}(E)$ was found to slightly increase with energy, such that $P_{conv}(85\text{ GeV})/P_{conv}(5\text{ GeV}) = 1.04 \pm 0.02$. This result is in agreement with data from the NIST database [174]. In the following, the photon conversion is studied using samples of almost monochromatic photons so that the energy dependence of $P_{conv}(E)$ has no noticeable effect on my measurements.

Figure 6.9 shows the amount of dead material in front of the BGO calorimeter, as viewed from the beam interaction point. The plotted distributions correspond to

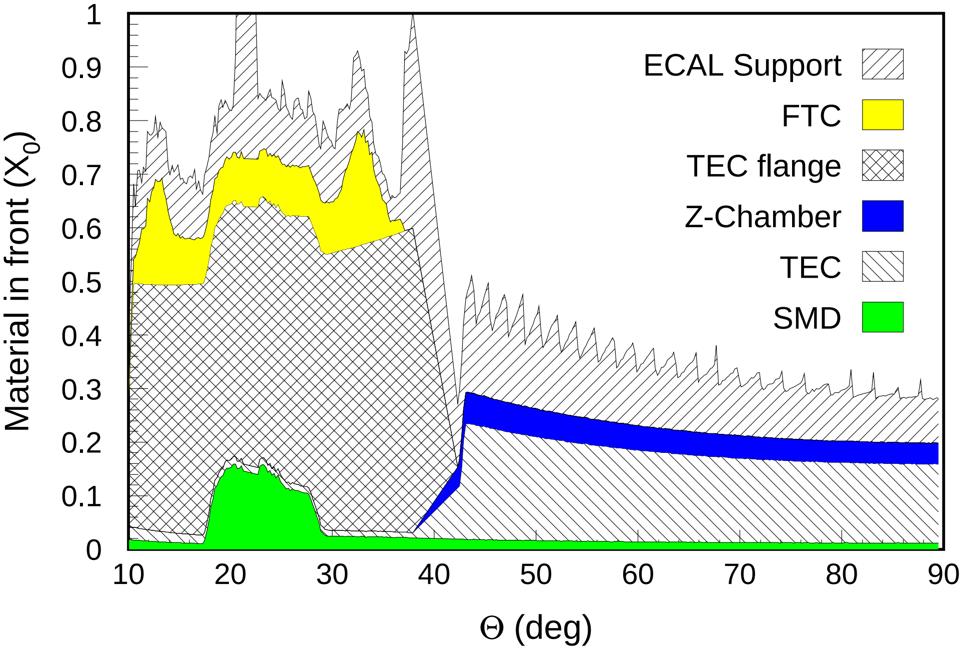

Figure 6.9: Plot of the amount of material in front of the BGO, measured in radiation lengths, as a function of the polar angle. Different layers show the contributions of various inner detector elements. Periodic variations in the amount of the BGO support material are due to steps used to support the individual crystals.

the structure of the L3 detector as used during the detector simulations.[11]

Most of the dead material was located in between the TEC and the BGO detectors. Thus, it did not lead to charged tracks in the TEC or to a significant deterioration of the energy resolution since the additional scattering and conversion were concentrated in a region just in front of the BGO crystals [172].

However, photons converted in the LEP beam pipe or in the silicon microvertex detector (SMD) would leave charged tracks in the TEC. According to Equation 6.4, the probability of such conversions was expected to be about 2% in the barrel region; it increased rapidly at low polar angles, reaching about 10% at $\theta \simeq 20°$. The sharp increase in the amount of dead material in front of the TEC at low polar angles, $\theta(180° - \theta) \simeq 15 - 25°$, was caused by the structure of the support system of the SMD (see Figure 6.9).

---

[11] This plot was provided by Dr. D. Kirkby [172] and is reproduced here with his permission.

The silicon microvertex detector was installed in 1993 and became fully operational in 1994, five years after the beginning of the LEP physics program. As a result, the Monte Carlo simulation of the detector did not provide a reliable description of the photon conversion in the SMD. Previous studies have found that, in most cases, the simulation tended to significantly underestimate the photon conversion rate [120, 175]. Below I investigate this problem separately for the endcap and the barrel regions of the BGO.

Photon Conversion in the Endcaps

Figure 6.10a shows the recoil mass distribution of the single-photon candidates in the endcaps passing all selection criteria except the cut on the TEC occupancy, $N_{hits}/N_{exp} < 0.4$. While the shape of this distribution is in agreement with the prediction, a clear discrepancy in the overall normalization can be seen. Most of the data events were observed in the region of the the Z-return peak ($M_{\mathrm{rec}} \simeq 91$ GeV), as was expected for single-photon events from the $\mathrm{e^+e^-} \rightarrow \nu\bar{\nu}\gamma$ process. The dominant background was predicted to come from the single-electron production in the four-fermion processes and the Bhabha scattering process. The M_{rec} distribution of the background was expected to be relatively flat. Therefore, I relaxed the TEC occupancy cut for the single-photon candidates in the endcaps with $80 < M_{\mathrm{rec}} < 130$ GeV.

I also used the selected sample of events with $M_{\mathrm{rec}} = 80 - 130$ GeV to estimate the photon conversion rate. The polar angle distribution of such events is shown in Figure 6.10b. The conversion rate was calculated as a ratio of the number of conversion candidates to the total number of single-photon events selected in this recoil mass window. As shown in Figure 6.10c, the Monte Carlo simulation substantially underestimated the conversion rate in the region of the SMD flanges, $\theta(180^\circ - \theta) < 25^\circ$. For $\theta(180^\circ - \theta) = 15 - 25^\circ$, the conversion rate was measured to be $R_{conv}^{DATA} = 18.7 \pm 2.1\%$, two times higher than the Monte Carlo prediction of $R_{conv}^{MC} = 9.3 \pm 0.1\%$. This result was in good agreement with the value of $R_{conv}^{DATA} = 15.1 \pm 2.6\%$, obtained by an independent study of the $\mathrm{e^+e^-} \rightarrow \mathrm{q\bar{q}}\gamma$ and $\mathrm{e^+e^-} \rightarrow \gamma\gamma$ processes[12] [175].

---

[12] In the study [175], a slightly tighter cut on the TEC occupancy was used.

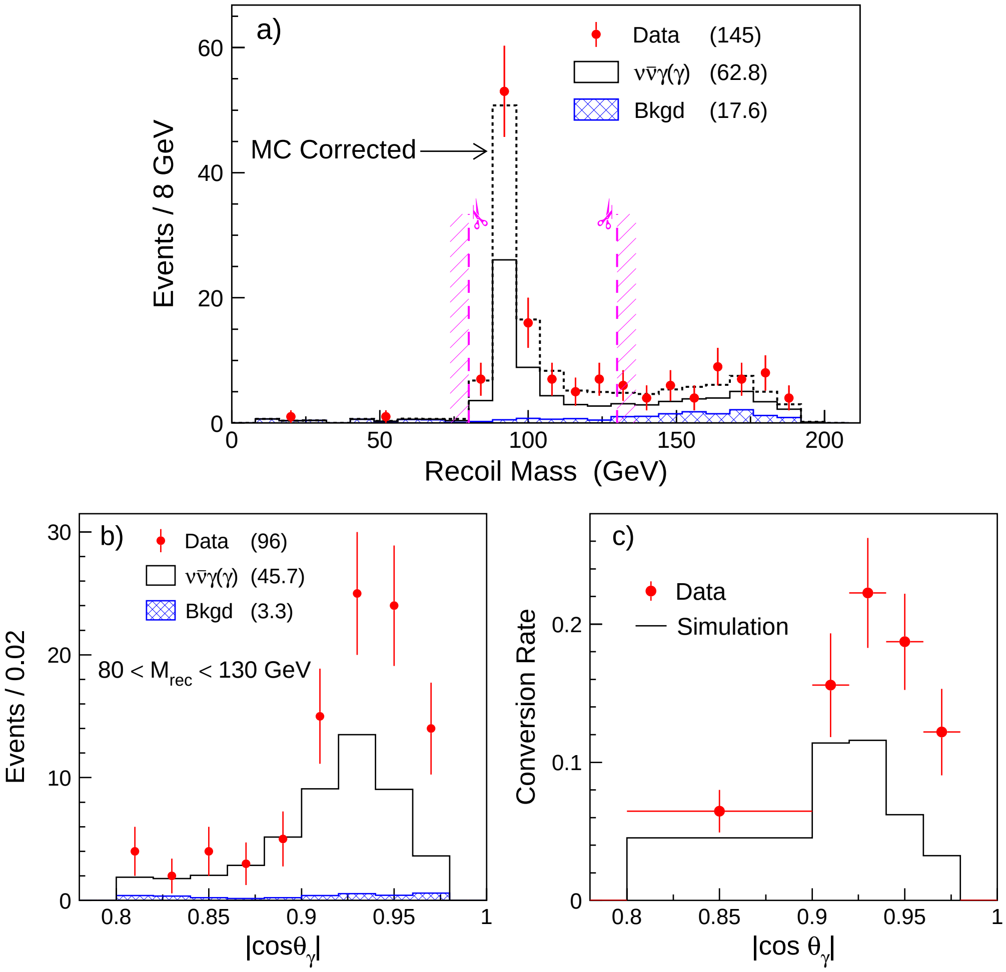

Figure 6.10: Distributions of a) the recoil mass for the single-photon events not passing the TEC occupancy cut and b) of the polar angle for events with $80 < M_{\rm rec} < 130$ GeV. c) Conversion probability as a function of the polar angle. The dashed histogram in plot a) shows the expected distribution after correction factors are applied. The event statistics are indicated on the plots.

The photon conversion rate, measured as a function of the polar angle (Figure 6.10c), was then used to correct the conversion rate in the simulation of the $\mathrm{e}^+\mathrm{e}^- \rightarrow \nu\bar{\nu}\gamma$ process. The recoil mass distribution of the conversion candidates in the endcaps was in good agreement with the corrected prediction, as shown in Figure 6.10a. The TEC occupancy cut was applied only in the region $M_{\rm rec} \neq 80 - 130$ GeV, where it rejected 49 events in data with 31 ± 3 and 14 events expected from the single-photon production and the background processes, respectively. As I discussed above, the events from the window $M_{\rm rec} = 80 - 130$ GeV were used for the measurement of conversion rate and, at the same time, were included in the selected sample of single-photon events. Therefore, the statistical and systematic errors in my measurement of the $e^+e^- \rightarrow \nu\bar{\nu}\gamma(\gamma)$ cross section became correlated (see Section 7.1). This effect was taken into account in the systematic error calculation and was found to be small compared to the total systematic error on the measured cross section.

Photon Conversion in the Barrel

In the barrel region, I studied the effect of photon conversion using events from the di-photon production process, $e^+e^- \rightarrow \gamma\gamma(\gamma)$. Such events were selected in the sample of events with two back-to-back BGO bumps which I used in the absolute calibration of the BGO calorimeter (the corresponding selection criteria were given in Section 5.6.2). The di-photon candidates were identified by requiring that at least one of the two photon candidates pass the cut on TEC occupancy, $N_{hits}/N_{exp} < 0.4$. In total, I selected 1,527 events in data with 1,568 and 26 events expected from the di-photon and Bhabha scattering processes, respectively. The numbers of selected and expected events were in good agreement with the published L3 results [158].

To measure the conversion rate as a function of the polar angle, I used the distribution of the polar angle of the event, shown in Figure 6.11a. Here, the polar angle of the event (θ^*) is defined as

$$\cos\theta^* = |\sin(\frac{\theta_1 - \theta_2}{2})/\sin(\frac{\theta_1 + \theta_2}{2})|, \tag{6.5}$$

where θ_1 and θ_2 are the polar angles of the two most energetic photons in the event.[13]

Events with one converted photon were further selected by requiring that the second photon candidate did not pass the cut on TEC occupancy. In total, I selected 161 such events in data with about 74 and 15 events expected from the di-photon and Bhabha scattering processes, respectively. The corresponding distribution of the polar angle of the event is shown in Figure 6.11b.

Denoting with R_c and N_0, respectively, the photon conversion rate and the number

---

[13] For events with perfectly back-to-back photons, $\cos\theta^* = |\cos\theta_1| = |\cos\theta_2|$.

of di-photon events in the preselected sample of events with back-to-back BGO bumps, the number of all di-photon events selected above and the number of events with one converted photon can be expressed as

$$N_{\gamma\gamma}^{tot} = N_0 \cdot (1 - R_c)^2 \,, \quad N_{\gamma\gamma}^{conv} = N_0 \cdot 2R_c(1 - R_c) \,. \tag{6.6}$$

Then, the photon conversion rate can be calculated as

$$R_c = \frac{r}{2 - r} \,, \text{ with } r = \frac{N_{\gamma\gamma}^{conv}}{N_{\gamma\gamma}^{tot}} \,, \tag{6.7}$$

where the values of $N_{\gamma\gamma}^{conv}$ and $N_{\gamma\gamma}^{tot}$ were obtained by subtracting the expected Bhabha background from the data. It should be noted that the above method was not very efficient for the region of the BGO endcaps due to much higher Bhabha background, which was caused by a rapid increase of the Bhabha cross section and a lower efficiency of the TEC.

Assuming that the thickness of the LEP beam pipe and the SMD detector was uniform in the barrel region, the angular dependence of the conversion rate would be given by a function $R_c(\theta) = R/\sin\theta$. Figure 6.11c shows that both for the data and Monte Carlo, the observed angular dependence was well described by this function. The fitted values of the parameter R were found to be equal to $R_{Data} = 4.3 \pm 0.4\%$ and $R_{MC} = 2.1 \pm 0.1\%$ for the data and Monte Carlo, respectively.

As was the case for the endcap region, the measured photon conversion rate was about two times higher than the prediction of the detector simulation program, $R_{Data}/R_{MC} = 2.1 \pm 0.2$. This value was in good agreement with previous studies of the photon conversion in the barrel, where it was measured to be $R_{Data}/R_{MC} = 2.5 \pm 0.4$ [120] and $R_{Data}/R_{MC} = 2.1 \pm 0.4$ [58]. Thus, in my samples of simulated single-photon events, I increased the fraction of events with converted photons in the barrel by a factor of 2.1.

The barrel region of the BGO calorimeter coincided with the most sensitive region of the L3 tracker ($\theta > 44°$), where the traversing charged tracks could be measured by

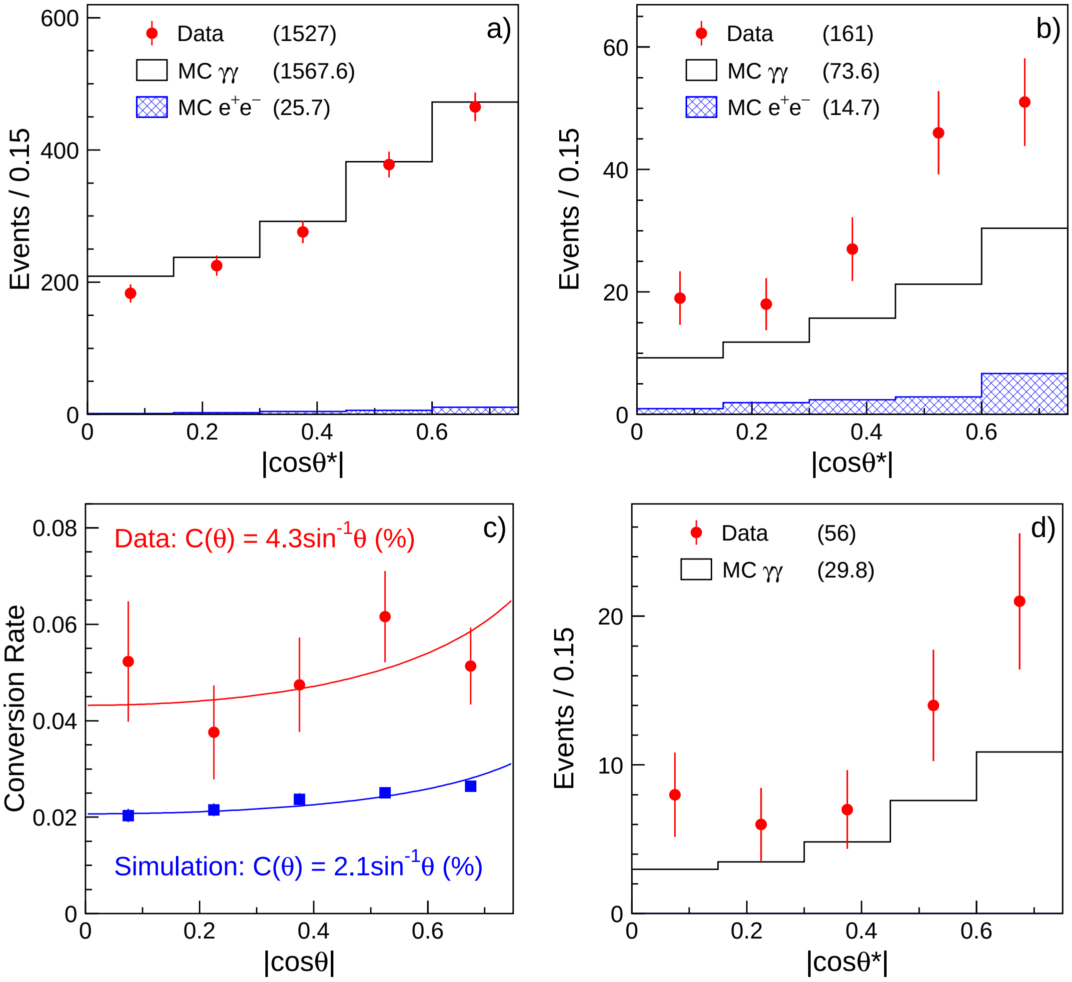

Figure 6.11: Distributions of $\cos\theta^*$ a) for all selected di-photon events, b) for events with one converted photon, and d) for events with two tracks matching to the converted photon; the event statistics are indicated on the plots. c) Photon conversion rate as a function of the polar angle.

all anode wires (see Section 4.2.2). Consequently, for a significant fraction of converted photons in the barrel, the two charged tracks of the produced e^+e^- pair could be resolved from one another. Such photon candidates, called "golden" conversions, were selected by requiring two matching tracks with an azimuthal opening angle $\Delta\Phi_{tracks} < 15^\circ$ (the quality criteria for the matching tracks were given in footnote 10 on p. 150). An example of a golden photon conversion is shown in Figure 6.8.

The distribution of the polar angle of the event for di-photon events with one golden converted photon is shown in Figure 6.11d. For 100 GeV photons, the fraction

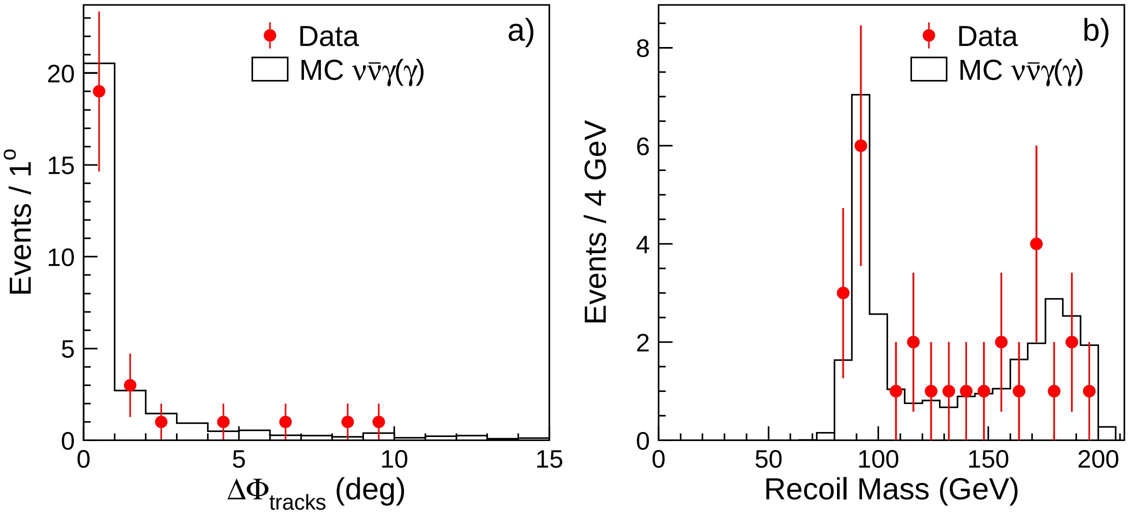

Figure 6.12: Distributions a) of the azimuthal angle between two matching tracks and b) of the recoil mass for the single-photon candidates accepted by the conversion selection in the barrel.

of golden conversions for 100 GeV photons was measured to be 38 ± 4%, which was in agreement with the Monte Carlo prediction of 40%. This result was also in good agreement with an earlier study of golden conversions [58].

Figure 6.11d shows that the real electrons could not fake the golden photon conversions. Therefore, I included such events in my selected sample of single-photon candidates in the barrel, i.e., for such events I relaxed the cut on TEC occupancy. In total, I selected 27 single-photon events with a golden conversion in the data with about 28.2 events expected from Monte Carlo. The distributions of the $\Delta\Phi_{tracks}$ variable and of the recoil mass for these single-photon candidates are shown in Figure 6.12.

Summary

I studied the effect of photon conversion using samples of events from the $e^+e^- \rightarrow \nu\bar{\nu}\gamma$ and $e^+e^- \rightarrow \gamma\gamma$ processes. The average conversion rates were determined to be about 13% and 5% in the endcap and barrel regions, respectively. The detector simulation program was found to significantly underestimate the amount of dead material in front of the L3 tracker, and the corresponding discrepancy in the conversion rate was taken into account.

By accepting single-photon events in the region of the radiative return to the Z (endcaps) and with golden photon conversions (barrel), I reduced the total efficiency loss caused by photon conversions to only about 2.8%. The above study represents the most accurate measurement of the photon conversion in L3 and is in good agreement with previous studies [58, 120, 175]. This allowed me to minimize the efficiency loss and the systematic uncertainties associated with this effect for my measurement of the single- and multi-photon production at LEP (see Section 7.1).

6.3.5 Cosmic Contamination

The earth's atmosphere is being continuously bombarded by a flux of high-energy particles, *primary cosmic rays*, which consists mainly of protons and heavier nuclei. Primary cosmic rays strike air molecules in the upper atmosphere, initiating an avalanche of secondary particles. Among the final products of such air showers, cosmic muons were of particular interest to LEP physics analyses.

The L3 detector was located 45 m underground and protected from the cosmic rays by about 30 m of solid rock. However, due to their relatively long lifetime of 2.2 μs and a relatively low rate of energy loss in matter, a significant fraction of cosmic muons with energies above 20 GeV reached the L3 detector.[14]

The cosmic muon events presented a source of unwanted background[15] for several L3 analyses, including my study of single- and multi-photon production at LEP. Cosmic muons traversing the BGO calorimeter could emit a bremsstrahlung photon and, thus, fake a single-photon event. The cosmic muons passed through the BGO

---

[14] For vertically incident cosmic muons, the mean energy loss to ionization in the rock overburden and in the L3 magnet corresponded to about 19 GeV [176].

[15] At the same time, a precise measurement of the cosmic muon flux is of great interest, as it allows one to predict the associated neutrino flux. At L3, such a measurement was performed with the upgraded setup of the L3 detector, known as L3+C [177]. It consisted of the L3 muon chambers, two arrays of scintillator counters installed outside the main L3 detector, and a dedicated trigger and data-acquisition system. In 1999-2000, the L3+C experiment recorded a total of 1.2×10^{10} cosmic muon triggers at an average trigger rate of 450 Hz. This resulted in one of the most precise measurements of the absolute muon flux for energies between 20 GeV and 3 TeV [176].

calorimeter at a rate of about 5 Hz [148]. Only a few percent of such events would be in coincidence with the beam-crossing window of LEP, and only a small fraction of muons would radiate a sufficiently hard photon in the BGO, since the bremsstrahlung cross section goes roughly as $1/\nu$, where ν is the fractional energy loss [6]. Nevertheless, each year thousands of cosmic ray events produced bremsstrahlung photons with an energy above 1 GeV in the BGO. In order to eliminate such events, I used a set of anti-cosmic cuts whose performance I describe below.

A picture of a cosmic ray event is shown in Figure 6.13. In this event, the cosmic muon entered the BGO calorimeter at a large angle with respect to the crystal axis and traversed about 30 crystals before radiating the bremsstrahlung photon. Since the photons were almost always emitted in the flight direction of the muon, the transverse profile of the resulting BGO shower would in general be oblong if the cosmic muon traversed the BGO at a significant angle to the crystal axis. Such cosmic ray events were then eliminated by the requirement that the shower roundness should be greater than 0.4 (see Section 6.3.1); for instance, the photon in Figure 6.13 had a roundness of 0.014. Thus, cosmic photons passing the cut on shower roundness were typically emitted by muons traversing the BGO calorimeter almost parallel to the crystal axis. The azimuthal distribution for such photons peaked at $\phi \simeq 90^\circ$ and $\phi \simeq 270^\circ$, as most of the cosmic ray muons were vertically incident.

Anti-Cosmic Cuts

The cosmic ray events did not originate from the beam collision, and their time of occurrence did not generally coincide with the beam crossing. Since the BGO calorimeter did not provide any timing information, the event time relative to the beam crossing was taken from the scintillation counters (time-of-flight system). As described in Section 4.2.4, the scintillation counters were located between the BGO and hadron calorimeters and had the timing resolution of 0.8 ns in the barrel and 1.9 ns in the endcaps. More than 99% of the cosmic ray events could be eliminated by a requirement that there should be at least one scintillator hit in time with the beam crossing within ±5 ns, $N_{scnt}(\pm 5 \text{ ns}) > 0$.

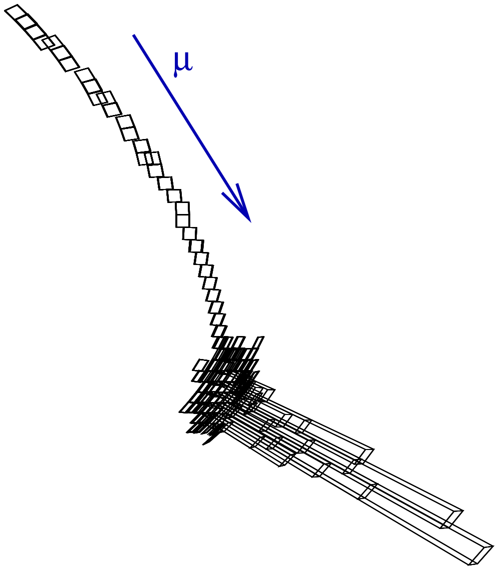

Figure 6.13: A typical cosmic ray event with a cosmic muon traversing the BGO calorimeter and emitting a bremsstrahlung photon.

For events with electrons or photons in the final state, the time-of-flight hits were produced by the shower particles emerging from the rear end of the BGO calorimeter. Because of this, I required that at least one in-time scintillator hit should be within a 15° cone around the direction of the photon. The longitudinal shower leakage decreased with shower energy, and so did the efficiency of this cut on the measured event time. To investigate the performance of this cut, I used control samples of tagged single-electron and back-to-back Bhabha events. These event samples were described in Sections 6.3.1 and 6.3.2, where they were used to study the performance of the shower-shape selection and the trigger efficiency. Because the single-electron events were tagged by a matching cluster in the forward calorimeters and the back-to-back Bhabha events had two bumps with an energy above $0.25\sqrt{s}$, these two event samples could be assumed to be virtually free of cosmic contamination.

Figure 6.14 shows the efficiency of the timing requirement, $N_{scnt}(\pm 5 \text{ ns}) > 0$, measured as a function of the shower energy. The fraction of showers satisfying this requirement increased from about 40% for $E_{shower} = 5$ GeV to about 99% for $E_{shower} = 45$ GeV. As a result, this cut would reject about 20% of the genuine single-

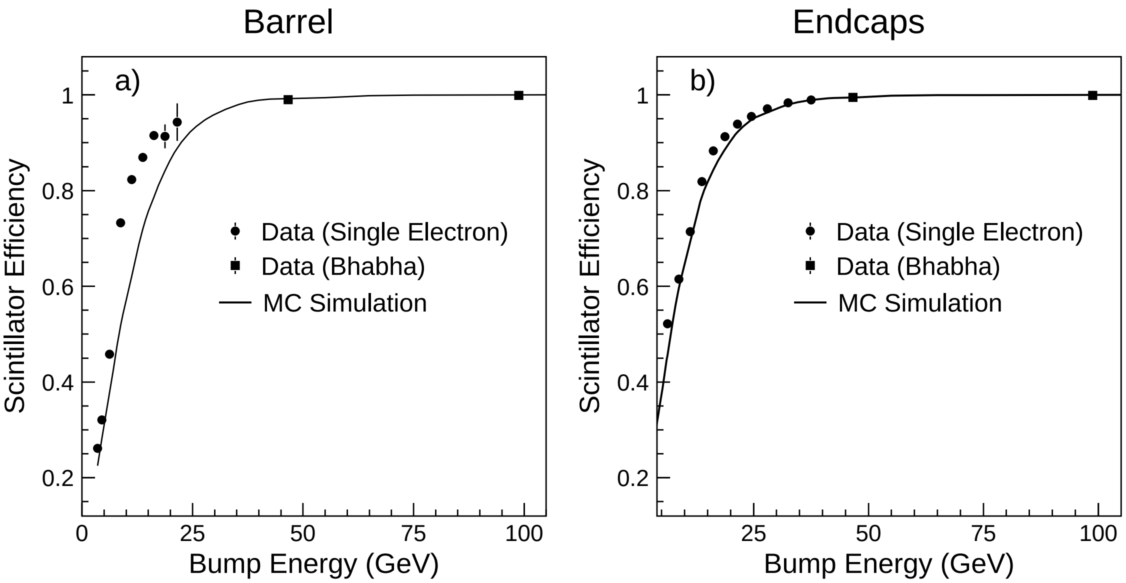

Figure 6.14: Scintillator efficiency as a function of the BGO shower energy a) for the BGO barrel and b) for the BGO endcaps.

photon events with $E_{shower} < 45$ GeV, which corresponded to the net efficiency loss of about 7%. Moreover, for showers with an energy below about 40 GeV, there is a noticeable discrepancy between the data and Monte Carlo. Since the longitudinal shower leakage was underestimated in the detector simulation (see the next section), the measured efficiency was significantly higher than the prediction of the detector simulation.

However, in the region $E_{shower} \geq 45$ GeV, a good agreement between data and Monte Carlo was observed. For 45 GeV Bhabha electrons, the scintillator efficiency was found to be about $99.15 \pm 0.07\%$ in the barrel and $99.49 \pm 0.04\%$ in the endcaps. These measured values were in good agreement with the Monte Carlo predictions of $99.24 \pm 0.04\%$ and $99.43 \pm 0.03\%$, respectively. For 100 GeV showers, the scintillator efficiency reached 99.9% both for the data and the detector simulation.

Therefore, in order to maximize the selection efficiency and minimize the associated systematic errors, I applied the timing cut of $N_{scnt}(\pm 5 \text{ ns}) > 0$ only to single-photon candidates with an energy above 45 GeV. For photons with lower energies, this cut was replaced by a requirement that there should be no scintillator hits more than 50 ns out-of-time with respect to the beam crossing ($T_{scnt} > 50$ ns). For such events, I also imposed an additional cut on the number of muon track segments.

The entire L3 detector was surrounded by a high-precision muon spectrometer, which consisted of three layers of drift chambers arranged in eight octants (barrel) and two endcaps (see Section 4.2.6). The design on the muon spectrometer was optimized for a detection of muons originating from the beam interaction point. Due to the presence of dead cells and inactive zones between the neighboring octants, only 90% of such muons would leave hits in at least two of the three layers of the muon chambers [118]. For cosmic muons the detection efficiency was expected to be even lower since they typically did not fly through the beam interaction region.

Thus, in order to reject a maximum possible fraction of the cosmic ray events, I required that there should be no muon track segments detected in any layer of the muon chambers, $N_{\mathrm{MUTK}} = 0$. Due to a significant level of noise in the individual drift chambers of the muon spectrometer,[16] this cut also eliminated about 3% of the genuine single-photon events (with $E_\gamma < 45$ GeV). This is a sizable loss of selection efficiency. However, it was much lower than if I had required the in-time scintillator hits for all single-photon candidates.

As I discussed above, most of the cosmic ray events that passed the cut on shower roundness were produced by cosmic muons traversing the BGO calorimeter nearly parallel to the crystal axis. Such cosmic muons would thus traverse two sides of the BGO calorimeter and produce a second BGO cluster in the hemisphere opposite to the bremsstrahlung photon, as shown in Figure 6.15.

Muons with an energy between several hundred MeV and several hundred GeV lose energy in matter primarily by ionization and atomic excitation. In this energy range, the mean rate of energy loss depends only slightly on the muon energy [6]. Thus, the total energy deposited by such a muon in the BGO calorimeter depended mainly on the length of the muon track in the BGO material. Muons from the LEP collisions traversed the full length of the crystal and deposited on average between 200

---

[16] This level of noise was much higher than for a typical muon selection of L3 as I did not require that there should be several muon track segments matching to each other.

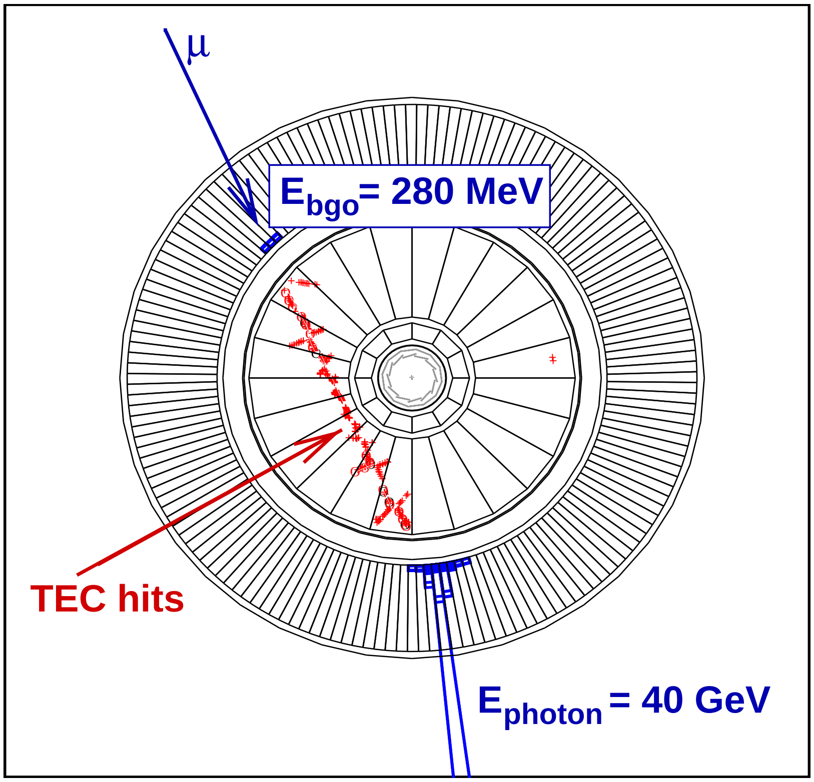

Figure 6.15: A typical cosmic ray event with a cosmic muon traversing the TEC before radiating a bremsstrahlung photon. The number of TEC hits in the 1 cm wide road between the photon candidate and the second BGO cluster was found to be equal to 136.

and 250 MeV [108]. For a cosmic ray muon, both the muon energy and the length of its track in the BGO could be substantially larger so that the energy deposited in the BGO could be as high as several hundred MeV.

Figure 6.15 shows that cosmic muons traversing two sides of the BGO would also leave a charged track in the TEC. Therefore, in order to further suppress the cosmic ray background, I applied the following cut: if there was a second BGO cluster with an energy $E_2 = 150 - 750$ MeV, no more than 20 hits should be found in the central tracking chamber in a 1 cm wide road between the photon candidate and the second BGO cluster, $N_{\mathrm{TEC}}(1 \text{ cm road}) \leq 20$. Since the TEC reconstruction algorithm was optimized to detect in-time tracks originating from the beam interaction region, I used a dedicated pattern-recognition algorithm that was developed specifically for the single-photon analysis at LEP1. More information on this algorithm can be found in Reference [173].

The above anti-cosmic cuts can be summarized as:

1. $N_{scnt}(\pm 5 \text{ ns}) > 0$ if $E_\gamma \geq 45$ GeV, or there should be no scintillator hits with $T_{scnt} > 50$ ns if $E_\gamma < 45$ GeV.
2. $N_{\text{MUTK}} = 0$ if $E_\gamma < 45$ GeV.
3. $N_{\text{TEC}}(1 \text{ cm road}) \leq 20$ if there was a second BGO cluster with an energy $E_2 = 150 - 750$ MeV.

Performance of the Anti-Cosmic Selection

To test the rejection power of the anti-cosmic cuts, I selected an independent sample of out-of-time cosmic ray events. First, I required that such events should contain at least one scintillator hit with 50 ns $< T_{scnt} <$ 700 ns with respect to the beam crossing. Second, I used the large difference between the 2 μs integration time of the BGO trigger system and the 11 μs integration time of the offline readout of the BGO (see Section 4.2.9). For in-time BGO showers, the ratio of the energy measured by the fast trigger ADCs (FERA) to the energy obtained from the offline reconstruction should be close to one, $E_{\text{FERA}}/E_{\text{BGO}} \simeq 1$. Therefore, to select only out-of-time cosmic events, I applied another cut: $0.15 < E_{\text{FERA}}/E_{\text{BGO}} < 0.5$. The out-of-time cosmic ray events were also required to satisfy all cuts of the single-photon selection except the anti-cosmic cuts. As a cross check, I applied the same selection to the control sample of 100,000 tagged single-electron events that was used to study the efficiency of the BGO triggers (see Section 6.3.2). No single-electron events were selected as out-of-time cosmic candidates.

Figure 6.16 shows the energy spectrum and the azimuthal angle distribution for photons in the selected out-of-time cosmic events. The energy spectrum is dominated by soft photons, as expected for a photon-bremsstrahlung process. The azimuthal distribution has clear peaks at $\phi_\gamma \simeq 90^\circ$ and $\phi_\gamma \simeq 270^\circ$ caused by the cut on shower roundness, as discussed above.

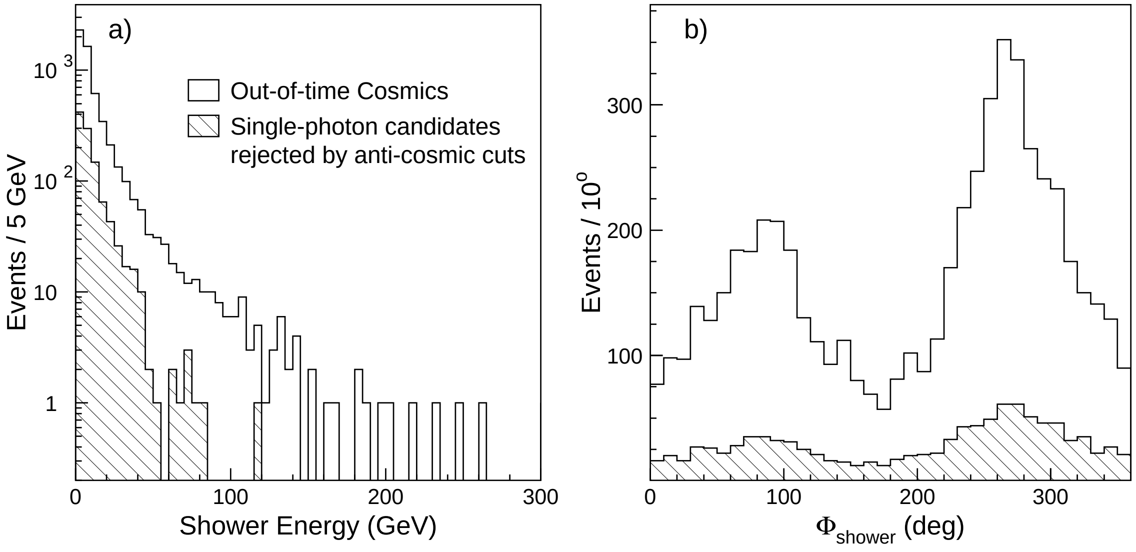

Figure 6.16: a) Energy and b) azimuthal distributions of the photons in the out-of-time cosmic ray events. Also shown are the corresponding distributions of the single-photon candidates rejected by the anti-cosmic cuts.

Next, I applied my anti-cosmic cuts on the number of muon track segments and on the number of hits in TEC to this sample of out-of-time cosmic events. Each of these two cuts was found to eliminate more than 90% of the out-of-time cosmic ray events. The rejection power of the anti-cosmic selection was then estimated as the ratio of the events not surviving these cuts to the total number of out-of-time events.

For the single-photon event topology ($P_t^\gamma > 0.02\sqrt{s}$ and $\theta_\gamma > 14°$), only 14 of the 3,745 out-of-time cosmic events survived the anti-cosmic cuts, corresponding to a rejection power of $P_{rej} = 99.6 \pm 0.1\%$. For the soft-photon event topology ($0.008\sqrt{s} < P_t^\gamma < 0.02\sqrt{s}$ and $\theta_\gamma > 43°$), 12 of the 2,010 out-of-time cosmic events survived the anti-cosmic cuts, corresponding to a rejection power of $P_{rej} = 99.4 \pm 0.2\%$.

The cosmic ray background in the final sample of single-photon events could then be estimated as

$$N_{\text{cosm}} = (1 - P_{rej}) \cdot (N_{\text{data}} - N_{\text{MC}})\,, \tag{6.8}$$

where N_{data} was the number of single-photon candidates selected in data before the application of the anti-cosmic cuts on the activity in the muon chambers and TEC, and N_{MC} was the corresponding Monte Carlo prediction for the Standard Model processes. These event numbers were found to be $N_{\mathrm{data}} = 2,629$ and $N_{\mathrm{MC}} = 1,957.2$, and the corresponding cosmic contamination was calculated to be $N_{\mathrm{cosm}} = 2.6 \pm 0.7$ events, which amounted to only about 0.1% of the final sample of single-photon events. For the soft-photon event topology, these event numbers were found to be $N_{\mathrm{data}} = 927$ and $N_{\mathrm{MC}} = 595.9$, which corresponded to a cosmic contamination of $N_{\mathrm{cosm}} = 2.0 \pm 0.6$ events.

As a cross check, I compared the energy and azimuthal distributions of the out-of-time cosmic ray events to the corresponding distributions of the single-photon and soft-photon candidates passing all selection criteria except the anti-cosmic cuts. As expected, the shapes of these distributions were found to be similar (see Figure 6.16).

Finally, for the multi-photon event topology ($E_{\gamma_2} > 1$ GeV), Equation 6.8 cannot be applied directly since no multi-photon candidates were rejected only by the anti-cosmic cuts. This is explained by the fact that the cosmic ray events rarely contained two sufficiently hard photons. Indeed, only 16 of the 5,769 out-of-time cosmic ray events had a second photon candidate with an energy above 1 GeV. None of these events survived the anti-cosmic cuts. For the multi-photon cosmic events, the rejection power of the anti-cosmic selection was expected to be about the same as for the single-photon cosmic events. Therefore, the cosmic contamination in the multi-photon channel could be assumed to be negligible.

6.3.6 Longitudinal Shower Leakage

As described in Section 6.3.1, photon candidates with significant shower leakage into the hadron calorimeter were rejected by requiring $E_{\mathrm{HCAL}}/E_{\mathrm{BGO}} < 0.2$, where E_{BGO} and E_{HCAL} were the energies measured in the BGO and HCAL calorimeters, respectively. Here, E_{HCAL} is defined as a sum of energies of the HCAL clusters in a 10° cone around the photon direction.

The $E_{\mathrm{HCAL}}/E_{\mathrm{BGO}}$ distribution for the 45 GeV Bhabha electrons (see Figure 6.3c) shows that the detector simulation substantially underestimated the effect of longitudinal shower leakage. This discrepancy was related to a poor description of the BGO support structure located in gaps between the BGO crystals. For Bhabha showers with significant leakage, the impact point was almost always found to be near the crystal edges, meaning that the leakage occurred mainly through the gaps between the crystals. The gap width varied from 200 μm to 900 μm *in situ*, but was fixed to a constant value of 200 μm in the Monte Carlo simulation [151].

This imperfection of the simulation program did not lead to a significant discrepancy in the efficiency of the shower-shape selection (see Section 6.3.1). However, the effect of longitudinal shower leakage had to be taken into account in order to avoid a systematic bias in the reconstructed photon energy.[17] To study this effect, I used the same samples of back-to-back Bhabha events as the ones that I used to study the performance of the shower-shape selection. While the average amount of shower leakage was measured to be quite small, $<E_{\mathrm{HCAL}}/E_{\mathrm{BGO}}> \simeq 0.8\%$, significant event-by-event fluctuations were observed and the ratio $E_{\mathrm{HCAL}}/E_{\mathrm{BGO}}$ was found to vary from zero to almost one (see Figure 6.3c).

To take into account energy losses caused by the longitudinal shower leakage, I developed a simple procedure that used the HCAL calorimeter as an improvised tail-catcher for electromagnetic showers. The corrected shower energy was calculated, on an event-by-event basis, as

$$E_{shower} = E_{\mathrm{BGO}} + \alpha \cdot (E_{\mathrm{HCAL}} - \beta \cdot E_{\mathrm{BGO}}) , \tag{6.9}$$

where the parameter α gave the response of the hadron calorimeter to electromagnetic clusters and the term $\beta \cdot E_{\mathrm{BGO}}$ represented the average shower leakage for Bhabha electrons used in the absolute calibration of the BGO calorimeter.[18] Because of significant differences in granularity and module design [87], the constants α and β were estimated separately for the barrel and the endcap regions of the HCAL. By

---

[17] The particle reconstruction algorithm of L3 calculated the energies of photons and electrons using information from the BGO calorimeter only, i.e., it assumed $E_{shower} = E_{\mathrm{BGO}}$.

[18] As described in Section 5.6.2 of Chapter 5, Bhabha electrons used in the absolute calibration of the BGO were required to satisfy $E_{\mathrm{HCAL}}/E_{\mathrm{BGO}} < 0.08$.

using the fact that the back-to-back Bhabha electrons were kinematically constrained to have an energy close to the beam energy, I obtained $\alpha = 1.25$ and $\beta = 0.6\%$ for the barrel region and $\alpha = 0.85$ and $\beta = 0.5\%$ for the endcap region. No significant differences were observed in the amount of relative shower leakage ($E_{\mathrm{HCAL}}/E_{\mathrm{BGO}}$) measured for the 45 GeV and 100 GeV Bhabha electrons.

For showers with low longitudinal leakage, the performance of this procedure suffered from contamination from random uranium and electronic noise in the HCAL. In addition, the HCAL response to low-energy electromagnetic clusters was not well understood. As a result, I found that my correction procedure was effective only for showers with $E_{\mathrm{HCAL}} > 3$ GeV.

The fraction of 100 GeV electrons with $E_{\mathrm{HCAL}} > 3$ GeV was measured to be about 6%. For such showers, the uncorrected energy measurement ($E_{shower} = E_{\mathrm{BGO}}$) was found to underestimate the true energy by 7% on average. Moreover, such significant shower leakage was found to degrade the relative energy resolution from 1% to about 5%. The correction procedure of Equation 6.9 not only corrected the absolute energy scale but also improved the relative resolution to about 2.5%.

I next applied this correction procedure to my single- and multi-photon candidates with $E_{\mathrm{HCAL}} > 3$ GeV and $E_{shower} > 40$ GeV. I found 89 such photon candidates in data corresponding to about 6.5% of the total sample of photons with $E_\gamma > 40$ GeV. Figure 6.17 shows that for such events the correction for leakage resulted in a clear improvement in the reconstruction of the Z-return peak. As I discuss in the next chapter, this was important for my measurement of the number of light neutrino species. I also applied the same correction procedure to my samples of simulated single-photon events, where the fraction of events with significant leakage was found to be only about 2.7%.

6.3.7 Detector Noise

The experimental signature of single-photon events was an electromagnetic shower and no other significant activity on the detector. This allowed me to reject background

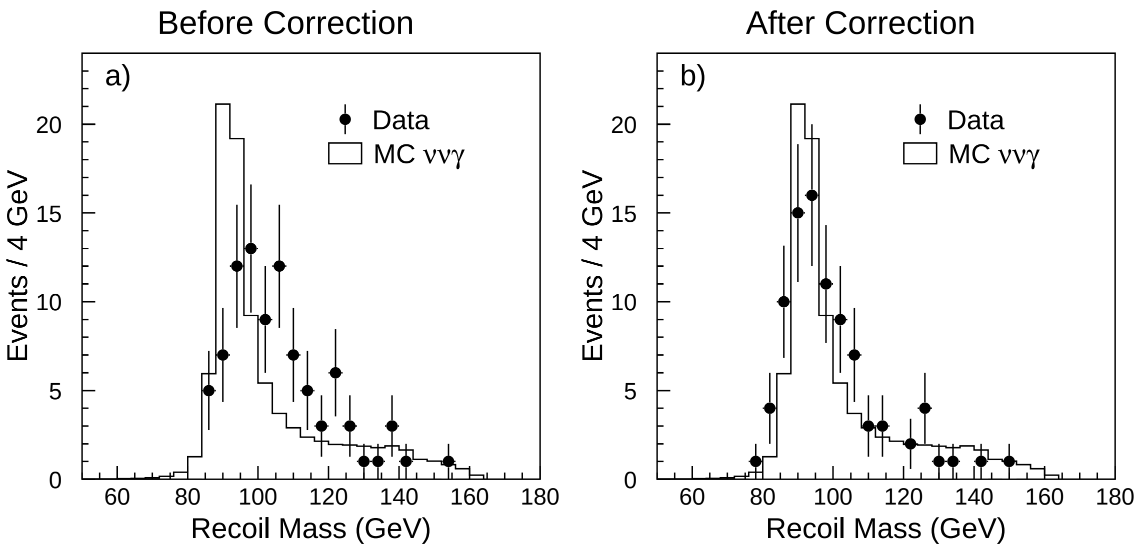

Figure 6.17: Recoil mass distribution for single-photon candidates with significant shower leakage into the HCAL, a) before and b) after the correction for leakage was applied. The data are compared to Monte Carlo prediction for single-photons with showers fully contained in the BGO calorimeter, where the Monte Carlo distribution was normalized to the number of data events.

events by using veto cuts on activity in various L3 subdetectors not associated with the identified photon candidate.

However, in the presence of detector noise, the veto cuts could also remove a sizable fraction of the genuine single-photon events. In order to study this effect, I used events randomly triggered at the beam crossing time. At L3, such events were obtained using a dedicated *beam-gate* trigger which accepted events at random time intervals based solely on the beam-crossing coincidence. The beam-gate events were collected at a rate of about 0.1 Hz, providing samples of about 500,000 beam-gate events per year of data-taking. I used these event samples to optimize the values of my veto cuts and to estimate the loss of selection efficiency (inefficiency) due to detector noise.

As mentioned in Section 6.3, all single-photon candidates had to satisfy the basic veto cuts which consisted of cuts on the following variables:

- Energy measured in the HCAL calorimeter $E_{\mathrm{HCAL}} < 7$ GeV

- Energy measured in the EGAP calorimeter $E_{\mathrm{EGAP}} < 7$ GeV
- Total visible energy (BGO+HCAL+EGAP) $E_{vis} < 10$ GeV
- Number of bumps in the BGO calorimeter $N_{bump} \leq 1$
- Number of good tracks[19] in the central tracker $N_{\mathrm{GTRK}} = 0$
- Number of good tracks[20] in the muon chambers $N_{\mathrm{muon}} = 0$.

Here, reconstructed objects matching to the identified photon candidates were excluded from the variables E_{HCAL}, E_{vis}, N_{bump}, and N_{GTRK}. Figures 6.18a-e show the corresponding distributions of the detector noise obtained using the beam-gate events from 1998-2000.

The inefficiency due to detector noise, associated with the basic veto cuts, was estimated to be only about 0.6%. As mentioned in Section 6.3.5, in order to suppress cosmic ray background I also required that there should be no muon track segments if the energy of the single-photon candidate was less than 45 GeV: $N_{\mathrm{MUTK}} = 0$ if $E_\gamma < 45$ GeV. For such events, the noise in muon chambers decreased the selection efficiency by about 3%. The distribution of the N_{MUTK} variable[21] for the beam-gate events is shown in Figure 6.18f.

Finally, to suppress background from radiative Bhabha events, I required that there should be no matching clusters in the forward calorimeters if the transverse momentum of the photon was less than 15 GeV, $P_t^\gamma < 15$ GeV (see Section 6.3.3). Specifically, I required that clusters in the ALR and LUMI calorimeters should satisfy $E_{\mathrm{ALR}} < 0.1$ GeV and $E_{\mathrm{LUMI}} < 1$ GeV if their acoplanarity with the photon candidate was less than 30°. Figure 6.19 shows that the level of noise in the forward calorimeters was relatively high[22] and, despite the acoplanarity requirement, this cut resulted in an additional loss of selection efficiency of about 0.9%.

---

[19] The quality criteria for good TEC tracks were given in footnote 10 on p. 150.

[20] The good tracks were required to have matching track segments in at least two of the three layers of the muon chambers.

[21] In the case of muon track segments, it was not always possible to resolve the left-right ambiguities, and the N_{MUTK} distribution had local maxima at even values of N_{MUTK} (see Figure 6.18f).

[22] In the forward calorimeters, the noise level was enhanced due to spurious beam-gas and beam-wall interactions and background from off-momentum beam-electrons [173].

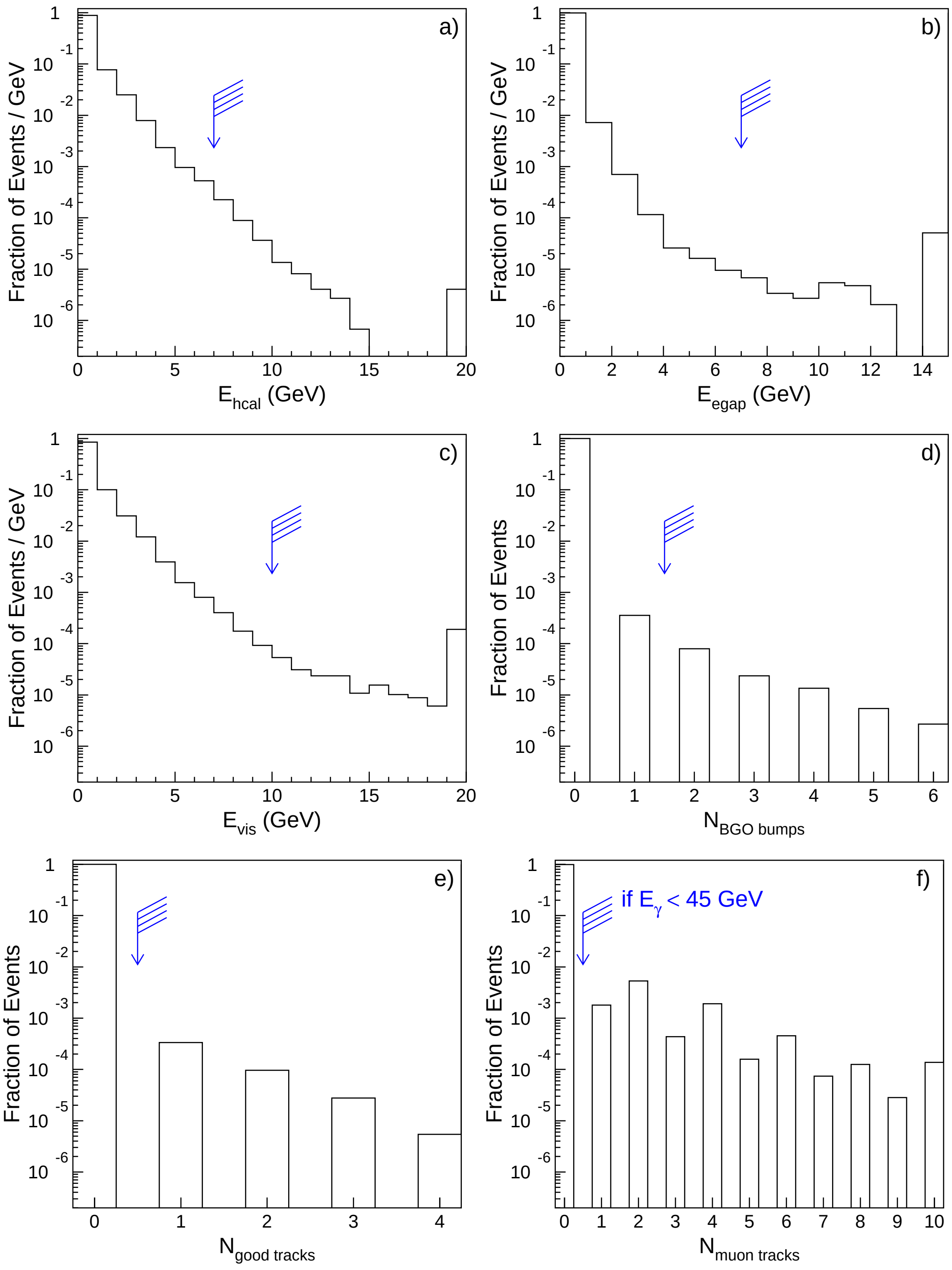

Figure 6.18: Distributions of the energies measured in a) the HCAL and b) the EGAP calorimeters, c) the total visible energy of the event, d) the number of BGO bumps, e) the number of good tracks in the TEC, and f) the number of tracks in the muon chambers for the 1998-2000 beam-gate event sample. The arrows indicate the values of the corresponding selection cuts. The last bin in each histogram contains the overflows.

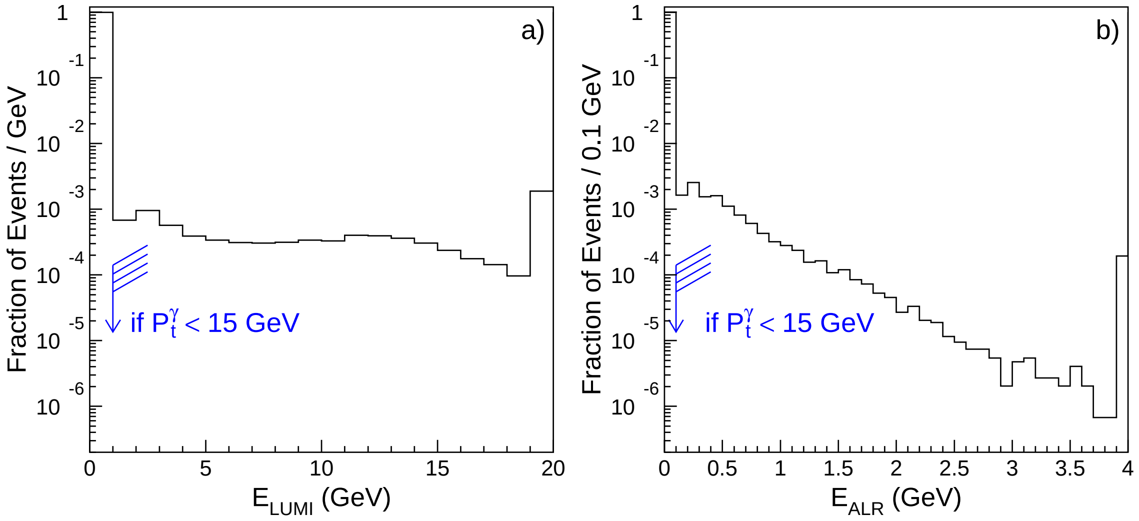

Figure 6.19: Distributions of the energies measured in a) LUMI and b) ALR forward calorimeters for the 1998-2000 beam-gate event sample. The arrows indicate the values of the corresponding selection cuts. The last bin in each histogram contains the overflows.

Since the beam-gate events were recorded at a constant trigger rate, the inefficiency due to noise in the detector was calculated as

$$\not{\epsilon}_{noise} = \sum_i \frac{\mathcal{L}_i \, n_i}{\mathcal{L} \, N_i}\,, \tag{6.10}$$

with $\mathcal{L}$ being the total luminosity, $\mathcal{L}_i$ the luminosity of the ith run,[23] N_i the total number of beam-gate events in the ith run, and n_i the number of beam-gate events in the ith run rejected by any of the above veto cuts. The obtained values of inefficiency are quoted in Table 6.4 for each of the four kinematic regions of my single-photon selection. The small year-to-year variations were taken into account.

As a cross check, I also measured the level of detector noise using the control samples of tagged single-electron and back-to-back Bhabha events. Such events had well-defined experimental signatures with few reconstructed objects in the detector and no activity expected in the outer subdetectors of L3 (HCAL and muon chambers). The obtained levels of noise in the individual subdetectors were found to be in

---

[23] Run is defined here as L3 data taken during an individual physics fill of LEP.

Kinematic Region	Fraction of Events	Inefficiency due to Detector Noise [%]		
		1998	1999	2000
$E_\gamma > 45$ GeV $P_t^\gamma > 15$ GeV	64.1%	0.51 ± 0.07	0.69 ± 0.06	0.70 ± 0.07
$E_\gamma > 45$ GeV $P_t^\gamma < 15$ GeV	0.6%	1.50 ± 0.07	1.53 ± 0.06	1.69 ± 0.07
$E_\gamma < 45$ GeV $P_t^\gamma > 15$ GeV	12%	3.61 ± 0.07	3.76 ± 0.06	3.47 ± 0.07
$E_\gamma < 45$ GeV $P_t^\gamma < 15$ GeV	23.2%	4.55 ± 0.07	4.54 ± 0.07	4.41 ± 0.07

Table 6.4: Inefficiency induced by the detector noise in 1998-2000 for the different kinematic regions of the single-photon selection. Also quoted is the fraction of events expected in each of the four kinematic regions.

agreement with those obtained using the beam-gate samples.

Averaging over the entire kinematic region of my single-photon selection gave an overall loss of selection efficiency of only about 1.9%.[24] The effects of the detector noise were completely ignored during the simulation of the detector response. To take into account such effects, I used a method described in Reference [173]. The detector simulation program of L3 assigned a run number to each simulated event according to the center-of-mass energy and the luminosity distribution of the LEP data. Then, for each Monte Carlo event, I randomly selected a beam-gate event from the same run in data and incorporated all reconstructed objects[25] from this beam-gate event into the original Monte Carlo event. The resulting loss of efficiency was found to be approximately the same as given by Equation 6.10 and Table 6.4.

6.3.8 Selection Results

A total of 1,921 events from the 1998-2000 data passed my single-photon selection. As described in Section 2.2.3 of Chapter 2, the Standard Model predictions for the single- and multi-photon production processes $e^+e^- \rightarrow \nu\bar{\nu}\gamma(\gamma)$ were obtained using the `KKMC` and `NUNUGPV` Monte Carlo generators. For the single-photon selection, the

---

[24] Due to optimization of the veto cuts, the resulting loss of selection efficiency was 2–4 times lower compared to other single-photon selections used in L3 at LEP1 and at the beginning of the LEP2 program [58, 120, 173].

[25] These included clusters in any of the calorimeters, as well as reconstructed tracks and individual hits in the TEC, SMD, and muon chambers.

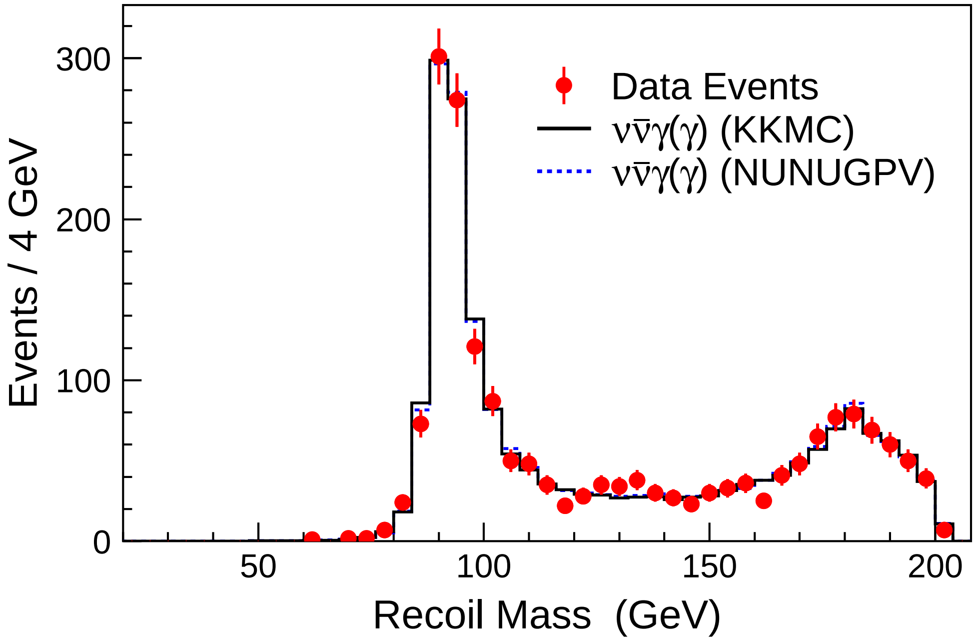

Figure 6.20: Recoil mass distribution of the single-photon candidates compared to the predictions of the `KKMC` and `NUNUGPV` Monte Carlo programs.

Monte Carlo expectations were found to be 1,917.5 events for `KKMC` and 1,930.7 events for `NUNUGPV`. The contributions from other sources were expected to give 15.2 events combined, including 8.3 events from the radiative Bhabha process $e^+e^- \to e^+e^-\gamma(\gamma)$, 3 events from the four-fermion processes $e^+e^- \to e^\pm\ell^\mp\nu_e\nu_\ell(\gamma)$ $(\ell = e, \mu, \tau)$, 1.3 events from the di-photon process $e^+e^- \to \gamma\gamma(\gamma)$, and 2.6 events from cosmic contamination.

Thus, the purity of the selected single-photon sample was estimated to be higher than 99%. For simplicity, in the following figures and tables, the Monte Carlo expectation from the all sources is denoted as expectation from the $e^+e^- \to \nu\bar{\nu}\gamma(\gamma)$ process.

The recoil mass $(M_{\rm rec})$ distribution of the single-photon candidates is shown in Figure 6.20 together with predictions from the `KKMC` and `NUNUGPV` generators. Good agreement between data and Monte Carlo predictions was observed over the entire range of $0 < M_{\rm rec} < \sqrt{s}$. This distribution peaked near the Z pole $(M_{\rm rec} \simeq M_Z)$ as explained in Section 2.2.2. In the region of the Z-return peak, $80 < M_{\rm rec} < 120$ GeV, 1,035 events were selected in data with 1,063.7 expected from the Monte Carlo (`KKMC`). The recoil mass of a photon candidate was calculated using its energy

		`KKMC`		`NUNUGPV`	
$\sqrt{s}$ (GeV)	Data	Expected	Efficiency[%]	Expected	Efficiency[%]
189	608	613.9	74.6 ± 0.2	613.5	74.8 ± 0.2
192	91	96.9	73.6 ± 0.2	98.8	74.2 ± 0.2
196	259	264.4	73.6 ± 0.2	265.1	73.9 ± 0.2
200	243	244.1	73.1 ± 0.2	249.0	73.7 ± 0.2
202	118	103.2	73.6 ± 0.2	104.9	73.5 ± 0.2
205	219	215.4	73.3 ± 0.2	216.9	73.7 ± 0.2
207	359	370.6	73.2 ± 0.2	373.4	73.6 ± 0.2
208	24	24.2	73.1 ± 0.2	24.3	73.4 ± 0.2
Total	1,921	1,932.7	73.7 ± 0.1	1,945.8	74.1 ± 0.1

Table 6.5: Summary of the single-photon selection giving (for each value of $\sqrt{s}$) the number of events selected in data together with the numbers of expected events and selection efficiencies calculated using the `KKMC` and `NUNUGPV` Monte Carlo programs, where the errors quoted are the statistical errors of the Monte Carlo samples.

(see Equation 6.1, p. 137), and the corresponding single-photon energy spectrum can be found in Figure D.1a (Appendix D). In addition, Figure D.2 shows the recoil mass distributions separately for each value of center-of-mass energy ($\sqrt{s}$).

The numbers of events selected at different $\sqrt{s}$ are listed in Table 6.5 together with the numbers of expected events obtained with the `KKMC` and `NUNUGPV` programs. Good agreement is observed both between data and Monte Carlo as well as between the predictions of `KKMC` and `NUNUGPV` within the 1% theoretical error quoted for these generators (see Section 2.2.3). In the following analysis, I will use Monte Carlo predictions obtained with the `KKMC` Monte Carlo generator.

Table 6.5 also lists the selection efficiencies calculated using the `KKMC` and `NUNUGPV` programs. Here, the selection efficiency is defined as the number of Monte Carlo events selected after the full simulation and all analysis cuts[26] divided by the number of events generated within the phase space of the single-photon topology, $14^\circ < \theta_\gamma < 166^\circ$ and $P_t^\gamma > 0.02\sqrt{s}$. The average selection efficiency was determined to

---

[26] Thus, here and in the following, quoted efficiencies include losses caused by noise in the detector and by inefficiency of the BGO trigger system.

be 73.7 ± 0.1% for `KKMC` and 74.1 ± 0.1% for `NUNUGPV`. In addition, the selection efficiency and the numbers of observed and expected events are provided in Table D.1 (Appendix D) in bins of $M_{\rm rec}$ and $|\cos\theta_\gamma|$.

The kinematic distributions of the single-photon candidates are shown in Figure 6.21. The distributions of the polar and azimuthal angles are shown in Figures 6.21a and 6.21b, respectively. The slight dips observed at $\phi_\gamma \simeq 90^\circ$ and $\phi_\gamma \simeq 270^\circ$ were mainly due to the RFQ holes in the BGO endcaps, and the slight dip at $\phi_\gamma \simeq 220^\circ$ was caused by a cluster of dead trigger cells in the BGO barrel. This structure of the azimuthal angle distribution was well reproduced by the Monte Carlo.

The transverse momentum distribution is shown in Figures 6.21c. The visible peak structures were caused by the phenomenon of the radiative return to the Z and by the gap between the BGO barrel and endcaps. This can be better understood by comparing Figures D.1b and D.1c (Appendix D) which show the transverse momentum distributions of the single-photon events in the BGO barrel and endcaps, respectively.

The trigger efficiencies and photon conversion rates were significantly different in the barrel and endcap regions (see Sections 6.3.2 and 6.3.4). It was therefore interesting to compare the observed and expected event rates separately for these two regions of my selection. In the BGO barrel, $\theta(180^\circ - \theta) > 43^\circ$, I selected 985 single-photon events in data with 971.6 expected from Monte Carlo. In the BGO endcaps, $14^\circ < \theta(180^\circ - \theta) < 37^\circ$, I selected 936 single-photon events in data with 961.1 expected from Monte Carlo. The recoil mass distributions of the single-photon candidates in the barrel and in the endcaps are shown in Figures 6.21d and 6.21e, respectively.

As shown in Figure 6.21a, the cross section of the reaction $\mathrm{e}^+\mathrm{e}^- \to \nu\bar{\nu}\gamma(\gamma)$ increased rapidly with decreasing $|\cos\theta_\gamma|$. Consequently, the numbers of single-photon events observed in the barrel and the endcaps were almost the same, even though the fiducial coverage of the BGO endcaps was about four times smaller than that of the BGO barrel. The selection efficiencies were found to be 81.9% for the barrel and 78.5% for the endcaps. These efficiencies are higher than the overall efficiency of my selection

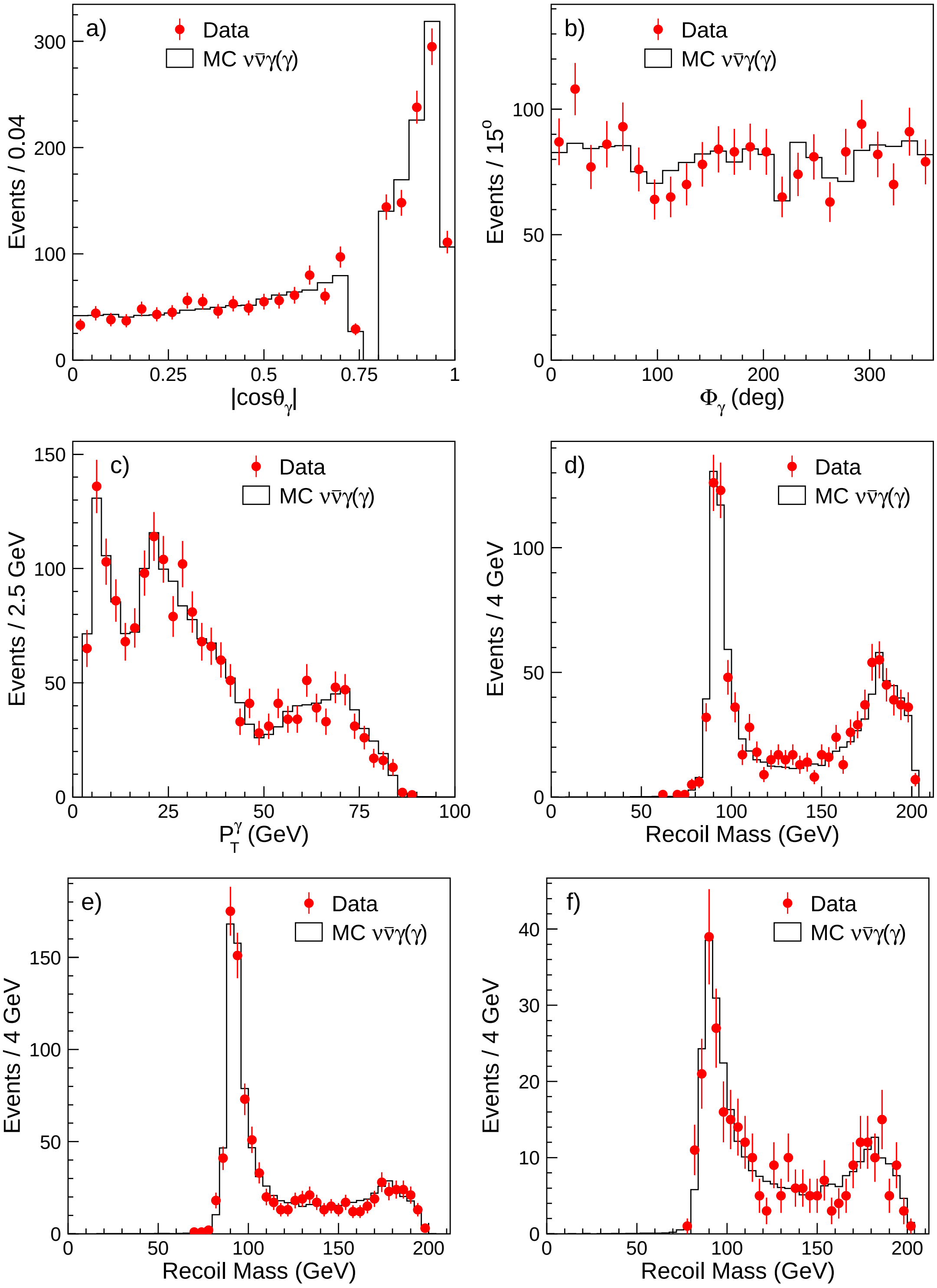

Figure 6.21: Distributions of a) the polar and b) the azimuthal angles and c) of the transverse momentum for the entire single-photon sample. Recoil mass distributions of the single-photon candidates d) in the barrel, e) in the endcaps, and f) near calorimeter edges or with dead channels in the shower.

(73.7%), which suffered from losses in the gaps between the barrel and endcaps of the BGO calorimeter.

As I have discussed in Section 6.3.1, photon candidates detected near the calorimeter edges or with a dead channel in the 3×3 crystal matrix were treated differently in my shower-shape analysis. In total, I selected 315 such single-photon events in data with 326.7 expected in Monte Carlo. The corresponding distribution of the recoil mass is shown in Figure 6.21f.

In summary, the observed event rates and kinematic distributions of my single-photon selection are found to be in good agreement with the Monte Carlo expectations. In the next chapter, I will use the selected sample of single-photon events to measure the cross section of the reaction e $e^+e^- \to \nu\bar{\nu}\gamma(\gamma)$ and to derive limits on deviations from the Standard Model in the framework of several new physics scenarios.

6.4 Multi-Photon Selection

As already mentioned in Section 6.2, multi-photon events with missing energy were defined as events with at least two photons, each with an energy above 1 GeV and a global transverse momentum $P_t^{\gamma\gamma} > 0.02\sqrt{s}$. In Section 2.2.2 of Chapter 2, I showed that the cross section of the multi-photon production process, $e^+e^- \to \nu\bar{\nu}\gamma\gamma(\gamma)$, should be about 15 times smaller than that of the single-photon production. The recoil mass[27] distribution is expected to have the familiar feature of the Z-return peak, and the energy spectrum of the second most energetic photon (E_{γ_2}) should be dominated by soft photons.

A multi-photon event recorded by the L3 detector is displayed in Figure 6.22. In my multi-photon sample, this event had the highest value of E_{γ_2} and therefore was one of the most interesting candidates for the process $e^+e^- \to YY \to XX\gamma\gamma$, where X and Y are new invisible particles. However, the recoil mass of this event was measured to be consistent with the Z mass, $M_{\mathrm{rec}} = 92.2$ GeV, indicating that this event was from the Standard Model process $e^+e^- \to \nu\bar{\nu}\gamma\gamma(\gamma)$.

---

[27] The recoil mass of a multi-photon event is calculated using Equation 6.1, p. 137.

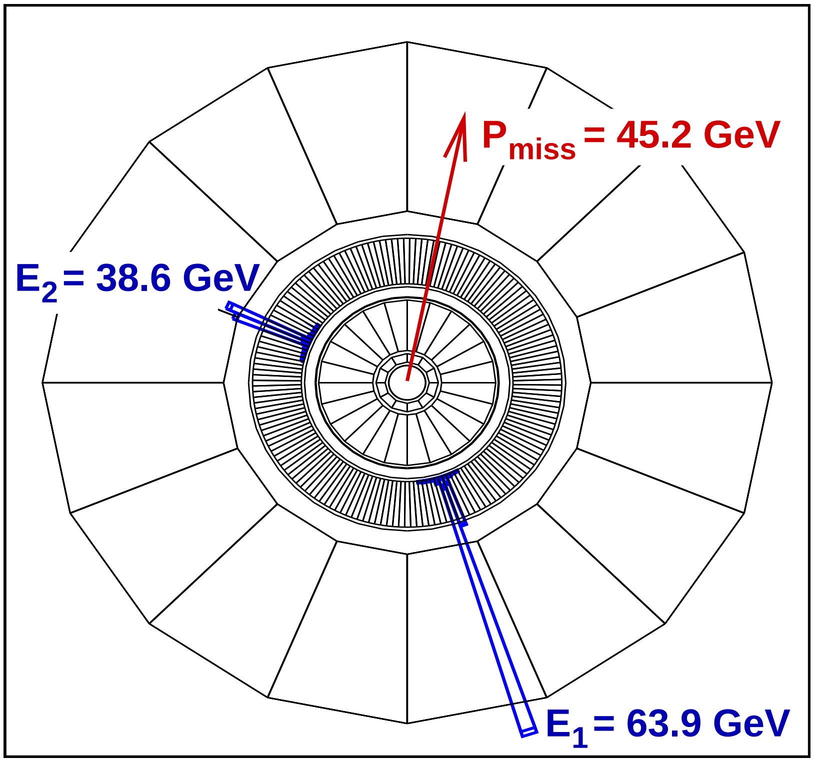

Figure 6.22: A multi-photon event recorded by the L3 detector, and displayed in the $x - y$ plane. This event was recorded in 2000 data at $\sqrt{s} = 205$ GeV.

Event Selection

The requirement of a second energetic photon in an event effectively eliminated backgrounds from cosmic ray events and from the radiative Bhabha and four-fermion processes which I had to consider in my single-photon analysis. On the other hand, it also significantly increased contamination from the di-photon process, $e^+e^- \rightarrow \gamma\gamma(\gamma)$.

Therefore, multi-photon events with missing energy were selected in a two-step procedure. In the first step, the veto cuts of the single-photon selection were applied[28] as defined in Sections 6.3 and 6.3.7. In addition, all photon candidates were required to pass the shower-shape cuts of Section 6.3.1 and the cut on TEC occupancy[29] of Section 6.3.4.

---

[28] For the clusters in the forward calorimeters, the acoplanarity angle was calculated with respect to the direction of the total momentum of the multi-photon system.

[29] Except for the golden converted photons in the barrel, which were also accepted.

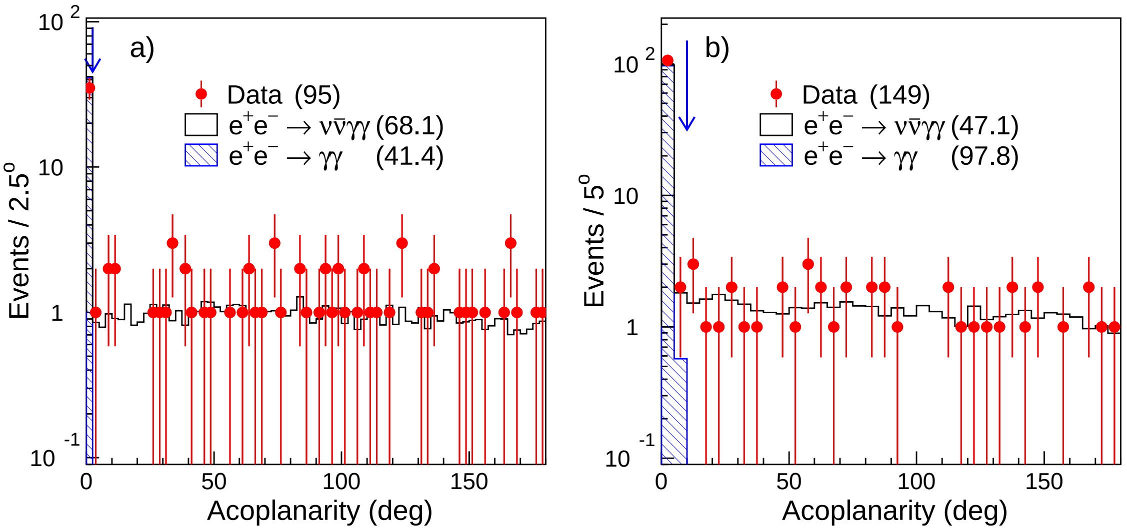

Figure 6.23: Distributions of the acoplanarity between the two most energetic photons after all other multi-photon selection cuts have been applied a) for events in which both photons were not near the calorimeter edges and did not contain dead channels and b) for events in which at least one of the photons did not satisfy these conditions. The arrows indicate the values of the cuts. The event statistics are also indicated on the plots.

After this preselection, 244 data events were retained with 254.6 expected from the Standard Model processes, including 115.3 events from the reaction $e^+e^- \to \nu\bar{\nu}\gamma\gamma(\gamma)$ and 139.2 events from the reaction $e^+e^- \to \gamma\gamma(\gamma)$. In order to further suppress the di-photon background, I required that the acoplanarity[30] between the two most energetic photons should be greater than 2.5°. About 20% of the photon candidates were detected near the calorimeter edges or had a dead channel in the 3×3 matrix centered on the most energetic crystal. For such showers, the uncertainty on the measurement of the photon direction was higher. Therefore I relaxed the acoplanarity cut to 10°, if an event contained at least one photon with dead or missing crystals in the shower. Figure 6.23 shows that this cut eliminated almost all di-photon contamination while retaining acceptance for $\nu\bar{\nu}\gamma\gamma(\gamma)$ events.

Finally, the remaining di-photon background was suppressed by requiring that the missing momentum vector should not point to the RFQ holes in the BGO endcaps. This cut eliminated 2 events in data with 1.4 expected from Monte Carlo.

---

[30] The definition of the acoplanarity angle was given in footnote 7 on p. 138.

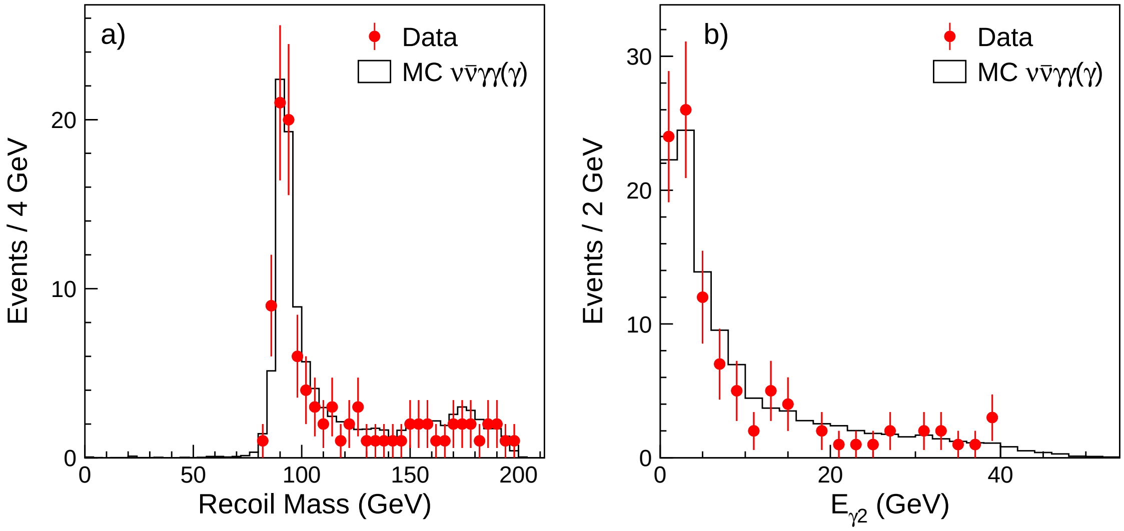

Figure 6.24: a) M_{rec} and b) E_{γ_2} distributions of the selected multi-photon events with missing energy.

Selection Results

The multi-photon selection applied to the 1998-2000 data yielded 101 events, in good agreement with the `KKMC` prediction of 111.6 events for the Standard Model $e^+e^- \rightarrow \nu\bar{\nu}\gamma\gamma(\gamma)$ contribution. The expected contribution for the di-photon background was found to be only 0.9 events and, for simplicity, in the following figures and tables it is added to the $\nu\bar{\nu}\gamma\gamma$ expectation. Figures 6.24a and 6.24b show, respectively, the M_{rec} and E_{γ_2} distributions of the selected multi-photon events with missing energy.

The numbers of events selected at different $\sqrt{s}$ are listed in Table 6.6 together with the numbers of expected events and the selection efficiencies obtained with the `KKMC` program. This table also lists the corresponding predictions for the `NUNUGPV` program, which was found to agree with `KKMC` within the the 5% theoretical error quoted for these Monte Carlo generators (see Section 2.2.3). Unless otherwise specified, in the following analysis I will use the predictions of `KKMC`.

The average selection efficiency, within the kinematic acceptance of this selection, was $57.1 \pm 0.4\%$. The efficiency of the multi-photon selection was significantly lower than that of the single-photon selection (73.7%) due to increased losses in the gaps

		`KKMC`		`NUNUGPV`	
$\sqrt{s}$ (GeV)	Data	Expected	Efficiency[%]	Expected	Efficiency[%]
189	26	35.3	58.5 ± 0.9	34.5	59.0 ± 0.7
192	11	5.6	58.6 ± 0.9	5.5	57.7 ± 0.7
196	17	15.2	56.2 ± 0.9	15.8	56.9 ± 0.7
200	15	14.5	56.9 ± 0.9	14.3	56.7 ± 0.7
202	3	5.9	55.9 ± 0.9	6.0	57.3 ± 0.7
205	10	12.6	55.2 ± 0.9	11.3	55.2 ± 0.8
207	17	22.1	56.7 ± 0.9	19.2	54.9 ± 0.8
208	2	1.4	55.7 ± 0.9	1.3	55.6 ± 0.8
Total	101	112.7	57.1 ± 0.4	107.8	56.9 ± 0.3

Table 6.6: Summary of the multi-photon selection giving (for each value of $\sqrt{s}$) the number of events selected in data together with the numbers of expected events and selection efficiencies calculated using the `KKMC` and `NUNUGPV` Monte Carlo programs, where the errors quoted are the statistical errors of the Monte Carlo samples.

between the barrel and endcaps of the BGO calorimeter. However, for the case when both photons were observed in the barrel of BGO calorimeter, the selection efficiency was determined to be 76.4%. This was important because most new physics signals were expected to be produced predominantly in the barrel region.

In Appendix D, Table D.2 gives the efficiencies of the multi-photon selection and the numbers of observed and expected events in bins of M_{rec} and E_{γ_2} for the full sample and for the case in which both photons were in the barrel. In addition, Figure D.3 shows the recoil mass distributions of the multi-photon events, separately, for each value of $\sqrt{s}$. The discussion of the results of the multi-photon selection will be continued in the next chapter, where I will use the multi-photon sample to search for signs of Supersymmetry and for anomalous quartic gauge-boson couplings.

6.5 Soft-Photon Selection

The soft-photon selection extended the transverse momentum range of the single-photon selection down to $P_t^\gamma = 0.008\sqrt{s}$ and covered only the BGO barrel region, where a single-photon trigger was implemented with a threshold around 1.5 GeV (see Figure 6.4b). Soft-photon events with missing energy were thus defined as events with only one photon with $43^\circ < \theta_\gamma < 137^\circ$ and $0.008\sqrt{s} < P_t^\gamma < 0.02\sqrt{s}$.

The selection of soft-photon events began by applying all cuts of the single-photon selection as described in Section 6.3. In this channel, most of the events were expected to come from the radiative Bhabha scattering process $\mathrm{e^+e^-} \to \mathrm{e^+e^-}\gamma$, in which both electrons were lost in the beam pipe and only a photon was scattered at a large polar angle. In order to reduce this background, I imposed the following additional cuts: no energy deposit was allowed in the forward calorimeters, there must be no other ECAL cluster with energy greater than 200 MeV, and the energy in the hadron calorimeter must be less than 5 GeV.

In total, 566 soft-photon candidates were selected in the 1998-2000 data with an expectation of 581.7, where 130 events were expected from the $\mathrm{e^+e^-} \to \nu\bar{\nu}\gamma(\gamma)$ process, 448.4 from the $\mathrm{e^+e^-} \to \mathrm{e^+e^-}\gamma(\gamma)$ process, 1.4 events from the two-photon $\mathrm{e^+e^-} \to \mathrm{e^+e^-e^+e^-}(\gamma)$ process, and 2 events from cosmic contamination. Figure 6.25 compares the energy spectrum and polar angle distribution of the selected soft-photon events with the Monte Carlo predictions. Good agreement between data and Monte Carlo was observed.

Table 6.7 gives the numbers of events selected at different $\sqrt{s}$, together with the numbers of expected events and the selection efficiencies (`KKMC`). In Appendix D, Figure D.4 shows the energy spectrum of the soft-photon candidates, separately, for each value of $\sqrt{s}$.

In the next chapter, I will use the results of the soft-photon selection in my searches for extra dimensions and pair-produced gravitinos.

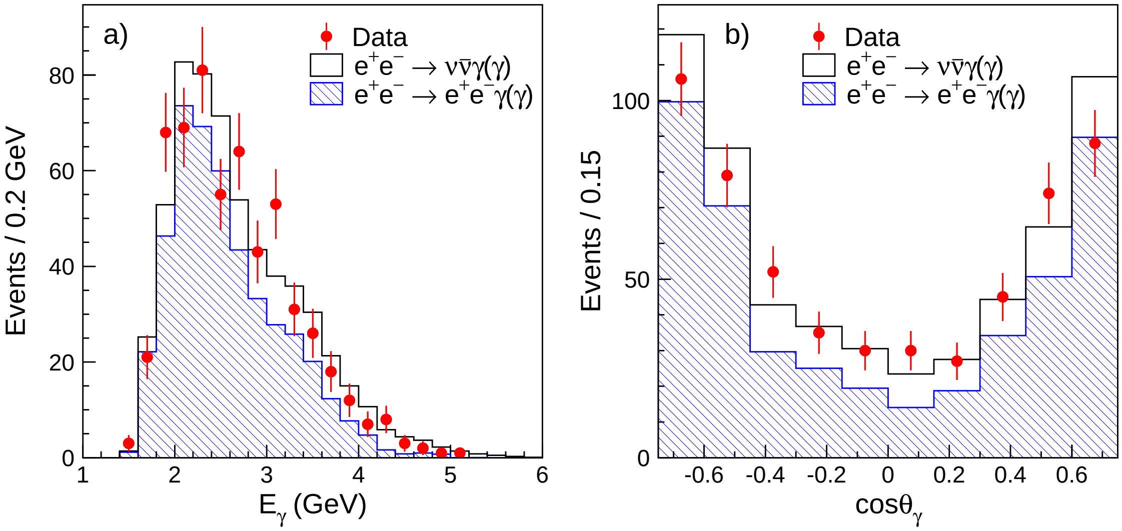

Figure 6.25: a) Energy spectrum and b) polar angle distribution of the soft-photon event sample.

$\sqrt{s}$ (GeV)	Data	Expectation			Efficiency[%]
		$\nu\bar{\nu}\gamma$	Background	Combined	
189	160	37.0	128.9	165.9	48.3 ± 0.8
192	34	6.3	23.6	29.9	49.8 ± 0.8
196	79	17.7	67.3	85.0	50.6 ± 0.8
200	77	16.8	63.5	80.3	50.1 ± 0.8
202	36	7.3	28.8	36.1	48.6 ± 0.8
205	74	15.8	49.0	64.7	51.9 ± 0.8
207	97	27.4	85.0	112.3	51.8 ± 0.8
208	9	1.8	5.6	7.4	52.2 ± 0.8
Total	566	130.0	451.7	581.7	50.1 ± 0.3

Table 6.7: Summary of the soft-photon selection giving (for each value of $\sqrt{s}$) the number of events selected in data together with the number of expected events and selection efficiency calculated using `KKMC`, where the errors quoted are the statistical errors of the Monte Carlo samples.